Probing Electron-Electron and Electron-Phonon Interactions in Twisted Bilayer Graphene

by

Isabelle Y. Phinney

Submitted to the Department of Physics
in partial fulfillment of the requirements for the degree of

Bachelor of Science in Physics

at the

MASSACHUSETTS INSTITUTE OF TECHNOLOGY

May 2020

© Massachusetts Institute of Technology 2020. All rights reserved.

Author . . . .
Department of Physics
May 8, 2020

Certified by . . . .
Professor Pablo Jarillo-Herrero
Thesis Supervisor, Department of Physics

Accepted by . . . .
Professor Nergis Mavalvala
Physics Associate Head, Department of Physics

Probing Electron-Electron and Electron-Phonon Interactions in Twisted Bilayer Graphene

by

Isabelle Y. Phinney

Submitted to the Department of Physics
on May 8, 2020, in partial fulfillment of the
requirements for the degree of
Bachelor of Science in Physics

Abstract

Two-dimensional systems, and, most recently, moiré systems, have risen to the forefront of condensed matter physics with the advent of experimental techniques that allow for controlled stacking of van der Waals heterostructures [17, 54]. For example, it was recently discovered that when two pieces of atomically thin carbon (graphene) are twisted at 1.1° with respect to one another, they display a variety of effects, including superconducting behavior [10]. Experimental investigation of the behavior of small-angle twisted bilayer graphene (SA-TBG) as a function of twist angle is imperative to understanding the mechanisms that play into the many interesting, strongly-interacting phenomena that the moiré system displays. In this thesis, I present three experiments which explore electron-electron and electron-phonon interactions in SA-TBG. I first consider SA-TBG as a host for a viscous electron fluid and look for the onset of fluid behavior via electron transport. Then I investigate the temperature dependence of resistivity in SA-TBG devices at a number of angles. The final experiment examines magnetophonons in three devices above the magic angle and compares the findings to theoretical results.

Thesis Supervisor: Professor Pablo Jarillo-Herrero

Acknowledgments

Over the past nearly two years, I have been extremely fortunate to work in the Jarillo-Herrero group at MIT. I would be remiss to not first acknowledge Professor Pablo Jarillo-Herrero for his support and generosity. Pablo was particularly kind in helping me through the graduate school application process, and I am deeply thankful. I would also like to thank Dr. Denis Bandurin for being the most supportive and patient mentor I could have ever hoped for. From teaching me to exfoliate graphene on day one to proofreading my fellowship application essays, Denis has been extremely generous with his time and has emphasized helping me develop as a physicist. He has taught me almost everything I know about experimental condensed matter, and I am extremely lucky and grateful to have him as a mentor. I would also like to thank all the members of the Jarillo-Herrero group for their support. I have learned so much from everyone in the group, and I am fortunate to call them both mentors and friends. Finally, I would like to thank my parents for always encouraging me to pursue my interests and for giving me many wonderful opportunities to do so.

Contents

1 Introduction and Background 21

1.1 Thesis introduction and motivation 21

1.2 Introduction to graphene 23

1.3 Twisted bilayer graphene 26

2 Experimental Techniques for SA-TBG Devices 29

2.1 The importance of high-quality devices 29

2.1.1 Doppler effect in graphene plasmons 30

2.1.2 THz-induced resistance oscillations 30

2.2 Device fabrication techniques 31

2.3 Measurement methods 34

2.3.1 Device characterization 37

2.3.2 Determining twist angle 41

3 Onset of Fluidity in TBG 49

3.1 Introduction - the graphene electron fluid and transport probes . . . 49

3.2 Background - regimes of electronic transport 51

3.2.1 Diffusive regime and the Drude model 52

3.2.2 Ballistic regime 53

3.2.3 Viscous regime and vicinity resistance 53

3.3 Results 54

3.4 Conclusion - competing interactions 57

4 Enhanced resistivity in SA-TBG 59

4.1 Introduction - temperature-dependent resistance in TBG 59

4.2 Background 60

4.3 Results 61

4.4 Conclusion - explanations for T^2 behavior 67

5 Observation of Magnetophonon Oscillations in TBG 69

5.1 Introduction - magnetophonons in graphene 69

5.2 Background 70

  5.2.1 A brief introduction to phonons 70

  5.2.2 Magnetophonon resonances in monolayer graphene 70

5.3 Results 72

5.4 Conclusion - inter-valley scattering 76

6 Conclusion and Future Directions 79

List of Figures

1-1 A visual summary of the experiments described in chapters 4-6. **Chapter 4**: Simulation of viscous flow in the graphene electron fluid. Adapted from [33]. **Chapter 5**: Data comparing resistivity versus temperature for monolayer, bilayer, and small-angle twisted bilayer graphene. **Chapter 6**: Cartoon depiction of electrons transitioning between Landau levels by emission of a phonon. 22

1-2 Graphene real-space and electronic structure [24] [41]. **a)** Cartoon depiction of six carbon atoms arranged in a honeycomb lattice. The p_z orbitals are indicated in blue and hybridize with the carbon atoms above and below the layer shown. The sp^2 orbitals, which form strong covalent bonds with neighboring carbon atoms, are indicated in pink. **b)** The honeycomb lattice of graphene with the inequivalent A and B sublattices labelled in purple and orange, respectively. A unit cell is highlighted in red. The unit vectors are defined as $a_1 = \frac{a}{2}(3, \sqrt{3})$ and $a_2 = \frac{3}{2}(3, -\sqrt{3})$, where a is the lattice constant of graphene. **c)** The first Brillouin zone of the reciprocal lattice is indicated in black with the K and K' points labelled. The reciprocal lattice unit vectors are defined as $\vec{a_i} \cdot \vec{b_j} = 2\pi\delta_{ij}$, giving $b_1 = \frac{2\pi}{3a}(1, \sqrt{3})$ and $b_2 = \frac{2\pi}{3a}(1, -\sqrt{3})$. **d)** The low-energy band structure for graphene as calculated by a tight-binding approximation and plotted in Mathematica. The red circle shows a close-up of the Dirac cones touching with a linear-in-energy dispersion. The conduction band (orange) and valence band (blue) are labelled. At zero doping, the Fermi energy, E_F, is located between the two bands. 24

1-3 Gating and the density of states in graphene. **a)** Graphene is a semimetal, meaning that charge can be added at no energy cost. Electrostatic gating is accomplished in a capacitor-like setup. In a typical device, the dielectric would be either silicon oxide or hexagonal boron nitride, and the gate would be either silicon, graphite, or palladium gold. **b)** The density of states in graphene, adapted from [41]. Note $\epsilon \propto n$, and that at zero doping ($n = 0$), the density of states goes to zero. **c)** Example resistivity data as a function of carrier density. At negative carrier density, the charge carriers can be thought of as positively charged holes. At $n = 0$, the resistivity exhibits a sharp peak—this can be thought of as a result of the zero DOS. For $n > 0$, the charge carriers are negatively charged electrons. 26

1-4 Basics of twisted bilayer graphene. **a)** A moiré pattern emerges as the twist angle is increased from 0. The blue arrows indicate the moiré lengthscale, $\lambda = a/2\sin(\theta/2)$. **b)** A low-energy continuum model of a SA-TBG system indicates that the Fermi velocity should be suppressed as the angle decreases, reaching 0 around 1.1°. Adapted from [5]. **c)** Overlapping Dirac cones in momentum space yield decoupling of the layers at low energies and van Hove singularities where the cones overlap, indicated by a black arrow. **d)** A line cut through the K points of the two lattices with a van Hove singularity indicated by a black arrow. Grey lines indicate the individual layers' Dirac cones before hybridization. 27

2-1 Steps of fabrication. **a)** A PC slide is mounted in a homemade transfer system. The selected hBN crystal exfoliated on Si/SiO$_2$ is placed in the transfer stage and heated to 50-70° C. **b)** The PC slide is lowered at an angle of 2-3°s and is used to pick up the hBN. **c)** The temperature of the stage is lowered to room temperature, and a large flake of monolayer graphene is placed on the stage. The flake may be pre-cut by laser, or may be torn in half during the transfer process. The edge of the hBN is used to define the tearing edge. **d)** The hBN and first piece of graphene on the PC slide are raised slightly above the stage, and the stage is rotated to the target angle. The PC slide is then lowered to pick up the second piece of graphene. **e)** We perform room temperature ironing by repeatedly pressing the hBN-graphene-graphene stack against the Si/SiO$_2$ substrate immediately after picking up the second graphene. **f)** The stack is released onto a prefabricated and cleaned hBN-graphite stack at 160-170° C. Ironing may be performed at high temperature during this step as well. 31

2-2 Images at various steps of fabrication for TBG-2.3°. **a)** Encapsulated twisted bilayer graphene. Bottom hBN (blue), top hBN (black), and twisted bilayer (red) after PC removal on a high-conductivity Si/SiO$_2$ substrate. Scale bar: 30μm. **b)** Dark field image of heterostructure with region examined via atomic force microscopy (AFM) indicated in red. Scale bar: 20μm. **c)** AFM image of regions used for Hall bar. Ripples are an artifact of the AFM and are not physical. White bar is 5 μm. **d)** Protective PMMA mask. Scale bar: 18μm. **e)** Contact regions after plasma etching. Si/SiO$_2$ substrate appears brown. Scale bar: 20μm. **f)** Contact regions after metal deposition and lift-off. Scale bar: 20μm. **g)** Hall bar after top gate is added and final etching. Scale bar: 15μm. h) Device bonded to ceramic chip carrier (gold-colored region: 2cm×2cm). 35

2-3 Measurement system. **a)** A Janis He-3 system with exchange gas. Our fridge is an older version of the diagram shown. Diagram from Janis Research. **b)** Four-terminal measurement configuration for determining the resistance of the channel. **c)** Hall effect measurement configuration. Magnetic field points out of plane. **d)** Bend resistance measurement configuration for measuring ballistic transport. **e)** Transverse magnetic focusing and vicinity resistance measurement configuration for studying ballistic transport and viscous flow, respectively. 36

2-4 Standard characterization measurements for TBG-2.2°. **a)** Comparison between the Dirac peak of TBG-2.2° and of monolayer graphene. Both are similarly narrow with a charge inhomogeniety on the order of $\delta n = 10^{10}\mathrm{cm}^-2$. This is a low charge inhomogeneity, likely due to the fact TBG-2.2° uses a graphite gate. **b)** Conductivity versus carrier density for electrons, plotted on a log-log scale. Where the red and blue lines intersect indicates δn, which matches with the width of the Dirac peak in a). **c)** Longitudinal (R_{xx}) resistance, plotted as a function of out-of-plane magnetic field and temperature (black to red). The low temperature oscillations are Shubnikov de Haas oscillations, which are suppressed as temperature is increased. Lower frequency magnetophonon oscillations become clearly visible at these higher temperatures. The Hall (R_{xy}) resistance at 4 K is plotted in blue on top. At higher magnetic fields, plateaus are visible in R_{xy}, corresponding to the filling of Landau levels. **d)** Mean free path for electrons, l_{mfp}, versus temperature T, calculated at a range of carrier densities, n, in TBG-2.2°. l_{mfp} is larger than or comparable to the device width up to 20 K for all carrier densities, demonstrating exceptional ballistic transport. **e)** Landau fan with fits to various filling factors plotted in pink. The Landau fan filling factor sequence for TBG will be (8N+4), double that of monolayer graphene. As a side note, magic angle TBG will have (4N+4). **f)** Landau fan for TBG-0.5°. A beautiful Hofstadter butterly pattern is visible, where we have added black lines to guide the eye. More experimental data is required to determine the exact angle of this device. 38

2-5 Data from ballistic characterization of SA-TBG devices. **a)** Transverse magnetic focusing for TBG-2.2°. Fits to equation 2.3 are plotted and show good agreement with the eight-fold degeneracy of TBG. **b)** Bend resistance for TBG-2.2°. 40

2-6 Fitting cyclotron mass with the Lifshitz-Kosevich formula for TBG-2.2°. **a)** Quantum oscillations at various temperatures with polynomial background removed. **b)** Normalized amplitudes versus temperature, fitted to Eq. 2.6 for three different values of B. **c)** m_c versus k_F, fitted assuming Dirac spectrum to find the Fermi velocity. Error bars are calculated as described in the main text. 41

2-7 Determining effective mass using FFT analysis for TBG-2.3° at $-4\,\mathrm{V}$ on the top gate. **a)** Raw resistivity data versus 1/B. **b)** Second derivative of data in **a)** to remove up to second order polynomial background. The purple indicates the region we select by hand to perform FFT on. **c)** FFT of purple region in **b)** with a Blackman window applied. The true B_F is the dip between the two peaks indicated. The double peak (black vertical lines) is a result of beating between SdHO and magnetophonons. **d)** We perform **b)** and **c)** four times, each time moving the purple window slightly to the left and right to double check that the effective mass and fundamental frequency do not shift with the choice of window. We fit the four windows and average to find the effective mass, 1.91×10^{-32} kg. 44

2-8 Alternate methods of determining twist angle. **a)** Longitudinal resistance versus backgate voltage (directly proportional to carrier density). The Dirac peak appears as a small peak on the right, and the superlattice gap appears as a tall peak on the left. **b)** $1/R_{xy}$ versus backgate voltage. The superlattice gap appears as a change in sign of $1/R_{xy}$. The slope of $1/R_{xy}$ near the two neutrality points can be used to determine the capacitance of the bottom hBN, as shown by the dashed lines. **c)** Brown-zak oscillaions (BZO) versus B-field. Black arrows indicate the peaks. Note the oscillations are periodic in $1/B$. **d)** Fit of the $1/B$ locations of the BZO peaks versus peak number. The slope gives the fundamental frequency. 46

3-1 Visualization of the three regimes of electronic transport in a vicinity resistance measurement configuration. **a)** In the ballistic regime, vicinity resistance is positive. **b)** Shear flow in the viscous electron fluid generates an electric field opposite to the direction of the applied electric field, and vicinity resistance is negative. **c)** Vicinity resistance is once again positive in the ohmic regime. **b)** and **c)** adapted from [33] 50

3-2 Characterization of TBG-2.2° and TBG-2.3°. Optical image of TBG-2.2°. **b)** Narrow Dirac peak for TBG-2.2°, indicating low charge inhomogeneity. The peak is narrower in carrier density than TBG-2.3°, most likely due to the fact that TBG-2.2° has a graphite backgate and TBG-2.3° has a PdAu topgate and Si bottom gate. Graphite has been shown to have lower charge disorder than metals and silicon. **c)** TMF for TBG-2.2°, showing ballistic transport over long distances. **d)** Optical image of TBG-2.3°. **e)** Narrow Dirac peak for TBG-2.3°. **f)** TMF for TBG-2.3°, showing ballistic transport over long distances. 55

3-3 Vicinity resistance versus temperature in SA-TBG. **a)** Top: vicinity resistance for monolayer graphene. Bottom: vicinity resistance for TBG-2.2°. Note that the regime of negative vicinity resistance in TBG-2.2° is much smaller in area, extending to a smaller extent in both n and T. Monolayer data adapted from [1]. **b)** Line-cut at $n = 0.25(10^{12}\,\mathrm{cm}^{-}2)$ for monolayer (blue) and TBG-2.2° (red). **c)** Longitudinal resistivity versus temperature for monolayer (blue), bilayer (green), and SA-TBG (red and orange) devices. Note that the SA-TBG devices show a much stronger increase in resistivity. 56

4-1 Device characterization for TBG-1.65° and TBG-0.5°. **a)** Optical image of TBG-1.65°. The Hall bar measured is the rightmost of the two shown. **b)** Narrow Dirac peak for TBG-1.65°. We do not currently know the origin of the small bumps on either side of the Dirac peak, but find they do not have a functional dependence on gating or magnetic field. **c)** TMF for TBG-1.65°. The apparent difference in quality between TMF for this smaller angle device in comparison to TBG-2.2° and TBG-2.3° is likely due to trigonal warping of the Fermi surface, which will be enhanced at smaller angles. The device also displays negative bend resistance, so we can be fairly confident that the device is ballistic at low temperature. **d)** Optical image of TBG-0.5°. We do not currently have enough data to determine the exact twist angle of the device. **e)** Narrow Dirac peak for TBG-0.5° as well as secondary peaks that are suppressed by increasing temperature. The large offset from zero may be due to a poor contact. **f)** Landau fan at 4 K displaying a Hofstadter butterfly. Black lines guide the eye. We do not yet have ballistic transport data for this device, but the cleanliness of the Landau fan indicates the device is of high quality. 62

4-2 Resistivity versus carrier density for a range of temperatures in five devices. **a)** $\rho_{xx}(T)$ vs. n for $T = 96$ to $T = 220\,\mathrm{K}$ in TBG-0.5°. Note that at low temperatures (Fig. 4-1), ρ_{xx} has several secondary peaks that are suppressed with temperature. **b)** $\rho_{xx}(T)$ vs. n for TBG-1.65° from 4 K to 280 K. Note this device reaches the highest values of resistivity and exaggerated thermal broadening. **c)** $\rho_{xx}(T)$ vs. n for TBG-2.2° from 4 K to 290 K. **d)** $\rho_{xx}(T)$ vs. n for TBG-2.3° from 4 K to 200 K. **e)** $\rho_{xx}(T)$ vs. n for TBG-4° from 4 K to 200 K. 63

4-3 Log-log plots of excess resistivity versus temperature for devices above the magic angle at a range of carrier densities. **a)** $\Delta\rho_{xx}$ vs. T for TBG-1.65° at a characteristic range of carrier densities for both electrons and holes. At lower temperatures, $\Delta\rho_{xx}$ follows a T^2 dependence, but saturates to a linear-in-T dependence at higher temperature, in agreement with [39]. **b)** $\Delta\rho_{xx}$ vs. T for TBG-2.2°, displaying a clear T^2 dependence for a wide range of carrier densities. **c)** $\Delta\rho_{xx}$ vs. T for TBG-2.3°, again displaying a strong T^2 dependence for a wide range of carrier densities. **d)** $\Delta\rho_{xx}$ vs. T for TBG-4°, displaying a T^2 dependence for smaller carrier densities and a super-linear dependence ($\approx T^{4/3}$) for larger carrier densities. 64

4-4 Summary of excess resistivity versus electron density and angle at $T = 100\,K$. $n = 1.8 \times 10^{12}\text{cm}^{-2}$ (black), $n = 1.5 \times 10^{12}\text{cm}^{-2}$ (red), $n = 1.0 \times 10^{12}\text{cm}^{-2}$ (green), $n = 0.5 \times 10^{12}\text{cm}^{-2}$ (blue). Note that the excess resistivity increases around the magic angle and decreases to either side, for larger and smaller angles. 66

5-1 Mechanisms for magnetophonon resonances in MLG and TBG. **a)** An electron scatters from a higher energy Landau level (LL) to a lower energy level by emission of a phonon with energy equal to the difference in energies of the LL. **b)** The same process but illustrated in real-space. An electron moving in a left-circularized cyclotron orbit jumps to a neighboring, right-circularized orbit by emission of a phonon with momentum equal to the electron's change in momentum. **c)** The mini Brillouin zone of SA-TBG with various quantities in k-space labelled. The distance between K_m and K'_m points of the mini BZ is $\frac{8\pi}{3a}\sin(\theta/2)$, a quantity that will be important to us later. 71

5-2 Magnetophonons versus Shubnikov de haas oscillations. **a)** $\partial\rho_{xx}/\partial B$ vs. $1/B$ as a function of temperature for $n = 2.77\times10^{12}\,\mathrm{cm}^{-2}$ for TBG-2.3°. SdHO are clear at low temperatures, appearing as sharp black and white vertical lines at the bottom of the map. As temperature is increased, lower frequency magnetophonon oscillations (MPO) appear. A linecut of $\partial\rho_{xx}/\partial B$ vs. $1/B$ at $T = 20\,K$ is shown in black. **b)** The normalized magnitudes of SdHO and MPO, obtained by FFT analysis, are plotted as a function of temperature. MPO occur over a much broader range of temperatures, but notably occur at low temperatures as well, at the same time as SdHO are present. **c)** $\partial\rho_{xx}/\partial B$ versus B as a function of I_{DC} at 20 K. The phase of MPO have been shown to be sensitive to an applied DC bias [59]. We see evidence of the phase shift as a function of the applied bias I_{DC} in the checkerboard pattern visible here. 73

5-3 Behavior of Magnetophonon resonances as a function of carrier density and inverse magnetic field for TBG-2.3° unless otherwise noted. **a)** SdHO at liquid-helium temperatures and MPO at 20 K vs. B. The difference in period is very apparent when plotted together. Black arrows indicate the peaks of MPO used to determine the fundamental frequency. **b)** MPO vs. $1/B$ plotted for comparatively high carrier densities, labelled on the right side of the graph. The resonant condition and the amplitude both show dependence on n. **c)** Peaks of MPO vs. peak number gives us the fundamental frequency B_F. $n = -2.2\times10^{12}\mathrm{cm}^-2$ (grey), $n = -2.8\times10^{12}\mathrm{cm}^-2$ (red), $n = -3.3\times10^{12}\mathrm{cm}^-2$ (green). **d)** FFT spectra of MPO, showing a decrease in amplitude as $|n|$ decreases. **e)** B_F vs $|n|$ for all three devices. B_F vs $|n|$ of monolayer graphene, obtained from [29], plotted in grey. The difference in functional behavior is apparent. 75

5-4 Phonon dispersions, both experimental and theoretically predicted. **a)** Phonon energy $\hbar\omega_{ph}$ vs. n, as measured. **b)** Low-energy phonon dispersion for layer-antisymmetric modes of 2.2° TBG from Ref. [25]. The linecut for q is taken between the Γ and K_m points. **c)** Phonon dispersion for bilayer graphene in the extended zone scheme along ΓK_m from Ref. [11]. Note the energy and momentum scales are different than in **b)**. 77

Chapter 1

Introduction and Background

1.1 Thesis introduction and motivation

Since the isolation of graphene in 2004 [18], two-dimensional (2D) systems have grown to become one of the primary research topics at the forefront of condensed matter physics [17, 54]. In recent years, moiré systems in particular have garnered great interest due to their experimental tunability and their ability to host a wide range of fascinating physical phenomena, which provide nanoscale accessibility to concepts in fundamental physics, astrophysics, quantum computing and more [9, 10, 53, 42]. The goal of this thesis is to further our understanding of the graphene moiré system in particular by considering the way electrons interact with each other and with other quantized modes in the system. The experiments described are some of many needed to understand, and later control, the many attractive moiré-induced phenomena found in these types of systems.

The following work is rooted in two main themes: 1) electronic transport in graphene, and 2) the twisted bilayer graphene moiré system. Graphene, one of the most common materials used in low-dimensional science, is composed of atomically thin layers of carbon and represents one of the best-known examples of a 2D layered material [18]. 2D layered materials are characterized by having much stronger in-plane bonds than out-of-plane, meaning that single layers can be physically removed from the bulk [54]. Furthermore, these layers can be stacked on top of other types of layered materials in any number of combinations. Such stacks are called van der Waals heterostructures, after the bonds that hold the layers together. The way in which these layers interact with each other—not just the atoms making up layers themselves—play a huge role in the physics of these structures. Twist angle can be used to change the way in which layers interact by the generatation of a moiré pattern. Moiré patterns are long wavelength interference patterns produced when two similar but slightly offset periodic patterns are laid on top of each other. We can realize this sort of pattern by stacking two identical layers of a crystal on top of one another with a relative twist angle, or by stacking two types of crystal with similar structure but slightly different lattice constant on top of one another. This thesis focuses on the way in which electronic transport is affected in small-angle twisted bilayer graphene (SA-TBG), a moiré system composed of two layers of graphene twisted relative to one another.

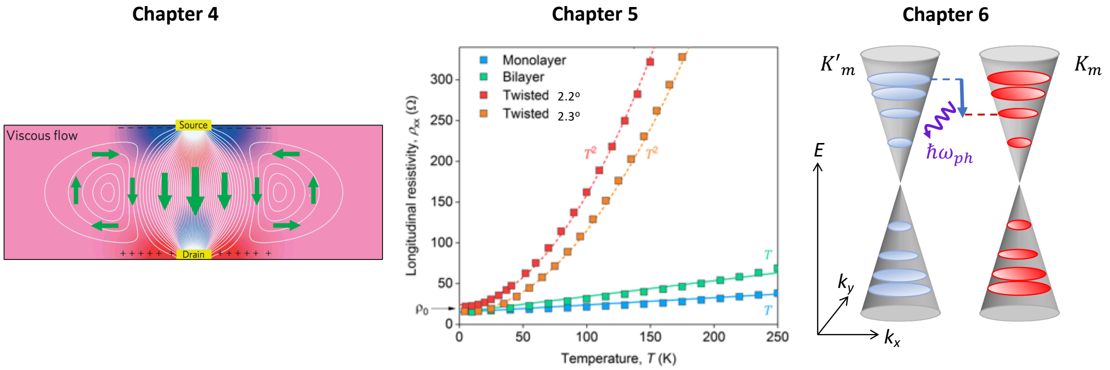

Figure 1-1: A visual summary of the experiments described in chapters 4-6. **Chapter 4**: Simulation of viscous flow in the graphene electron fluid. Adapted from [33]. **Chapter 5**: Data comparing resistivity versus temperature for monolayer, bilayer, and small-angle twisted bilayer graphene. **Chapter 6**: Cartoon depiction of electrons transitioning between Landau levels by emission of a phonon.

In chapter 1, I give an introduction to van der Waals heterostructures, graphene, and SA-TBG in particular. In chapter 2, I discuss fabrication and measurement methods. I emphasize the importance of high quality fabrication techniques by summarizing two collaborative projects to which I contributed devices. I also describe device characterization methods relevant to the particular experiments performed. In chapter 3, I give an introduction to hydrodynamics in graphene systems and present data showing the onset of fluidity in SA-TBG devices. I discuss the observation of a competing interaction, which leads into chapter 4, where I present resistivity versus temperature measurements. In chapter 5, I describe experiments on magnetophonons in SA-TBG and provide a possible explanation for the phenonema observed in chapters 3 and 4. Finally, in chapter 6, I briefly review the topics discussed and provide an outlook for future experiments.

1.2 Introduction to graphene

With the Nobel prize-winning isolation of graphene and demonstration of its unique electrical properties in 2004 by Professors Andre Geim and Konstantin Novoselov [18], a whole new two-dimensional world became readily available to physicists. Today, condensed matter has expanded to explore other materials in the low-dimensional limit, including 2D superconductors, topological insulators, and more, bringing advances to both physics and technology [54, 42, 43]. However, graphene continues to be an invaluable platform to study strongly-interacting phenomena, most recently with the demonstration of superconductivity in twisted bilayer graphene [10]. The long-lived productivity of graphene physics can be attributed to two things: first, graphene has many unusual features, including a gapless Dirac band structure, weak electron-phonon coupling, and high electron mobility [18]. Moreover, it boasts the experimental advantages of being cheap, easy to procure, and highly stable.

Graphene is composed of carbon arranged in a hexagonal “honeycomb” lattice. Carbon has the electron configuration [He]$2s^2 2p^2$. The p_x, p_y, and s orbitals mix to form three hybridized σ bonds which are oriented in-plane and combine with neighboring carbon atoms to form extremely strong covalent bonds, shown in Fig. 1-2a. The p_z orbital forms an out-of-plane π bond that is responsible for the low energy electronic states in graphene. As shown in Fig. 1-2b, the honeycomb lattice is in fact composed of two inequivalent triangular sublattices, labelled A and B. In momentum

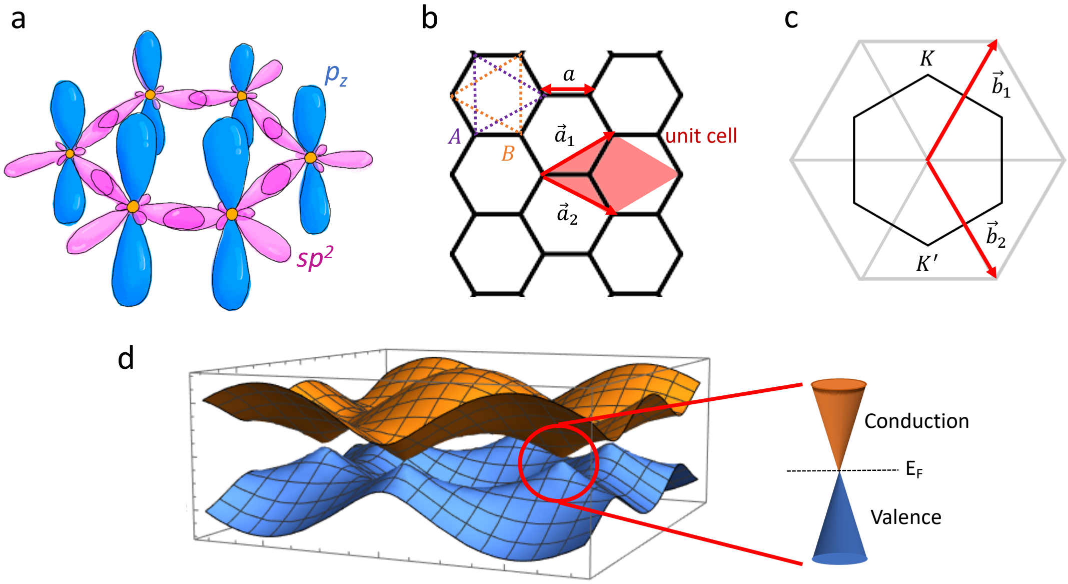

Figure 1-2: Graphene real-space and electronic structure [24] [41]. **a)** Cartoon depiction of six carbon atoms arranged in a honeycomb lattice. The p_z orbitals are indicated in blue and hybridize with the carbon atoms above and below the layer shown. The sp^2 orbitals, which form strong covalent bonds with neighboring carbon atoms, are indicated in pink. **b)** The honeycomb lattice of graphene with the inequivalent A and B sublattices labelled in purple and orange, respectively. A unit cell is highlighted in red. The unit vectors are defined as $a_1 = \frac{a}{2}(3, \sqrt{3})$ and $a_2 = \frac{3}{2}(3, -\sqrt{3})$, where a is the lattice constant of graphene. **c)** The first Brillouin zone of the reciprocal lattice is indicated in black with the K and K' points labelled. The reciprocal lattice unit vectors are defined as $\vec{a_i} \cdot \vec{b_j} = 2\pi\delta_{ij}$, giving $b_1 = \frac{2\pi}{3a}(1, \sqrt{3})$ and $b_2 = \frac{2\pi}{3a}(1, -\sqrt{3})$. **d)** The low-energy band structure for graphene as calculated by a tight-binding approximation and plotted in Mathematica. The red circle shows a close-up of the Dirac cones touching with a linear-in-energy dispersion. The conduction band (orange) and valence band (blue) are labelled. At zero doping, the Fermi energy, E_F, is located between the two bands.

space, the reciprocal lattice is also hexagonal, where we now label the inequivalent points K and K' (Fig. 1-2b).

A simple tight-binding picture captures many of the important electronic features of the system. The band structure shows that, at the corners of the Brillouin zone (BZ), the conduction and valence band touch (Fig. 1-2d). The six high symmetry points are typically called Dirac points, divided into two inequivalent sets labelled K and K'. Expanding around the Dirac points as in Fig. 1-2d, we obtain a linear energy dispersion, $E(k) = \pm\hbar v_F k$, where $\hbar$ is the reduced Planck's constant, v_F is the Fermi velocity, approximately 10^6 m/s in monolayer graphene. Notably, the energies of the Dirac points are degenerate, so we often simply assign the two degenerate valleys a quantum number. Including spin as another good quantum number, we get a four-fold degenerate Dirac cone.

The linear spectrum near the Dirac points results in a few interesting features. The first is that the typical definition for effective mass, $m^* = \frac{\hbar^2}{\partial^2 E/\partial k^2}$ breaks down because of the linear, rather than parabolic, energy spectrum. Instead, we chose to define the effective mass as the cyclotron effective mass in graphene. The cyclotron effective mass is semiclassically defined by $\omega_c = \frac{eB}{m_c c} = \frac{\hbar^2}{2\pi}\frac{\partial A}{\partial E}$, where A is the area in k-space enclosed by the cyclotron orbit. In graphene, which has an isotropic energy spectrum, we get

$$m_c = \frac{\hbar^2}{2\pi}\frac{\partial A}{\partial k}\frac{\partial k}{\partial E} = \frac{\hbar k}{v_F} \tag{1.1}$$

Experimentally, we can obtain the value for m_c by inspecting effects that depend on cyclotron motion, such as cyclotron resonance or Shubnikov de Haas quantum oscillations (see chapter 2).

Another handy feature of graphene is the ability to change the carrier density, n, by electrostatic gating. Since the conduction and valence bands touch, graphene has no band gap, meaning that charge can be added to the system with no energy cost. We accomplish this using a capacitor-like setup with graphene separated from a gate electrode by a dielectric (Fig. 1-3a). A voltage is applied between graphene and the gate. We see the effects of the Dirac cones as we vary the voltage between the two:

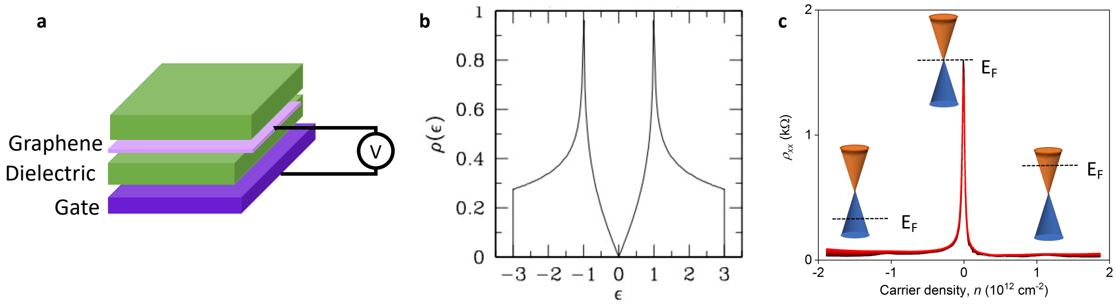

Figure 1-3: Gating and the density of states in graphene. **a)** Graphene is a semimetal, meaning that charge can be added at no energy cost. Electrostatic gating is accomplished in a capacitor-like setup. In a typical device, the dielectric would be either silicon oxide or hexagonal boron nitride, and the gate would be either silicon, graphite, or palladium gold. **b)** The density of states in graphene, adapted from [41]. Note $\epsilon \propto n$, and that at zero doping ($n = 0$), the density of states goes to zero. **c)** Example resistivity data as a function of carrier density. At negative carrier density, the charge carriers can be thought of as positively charged holes. At $n = 0$, the resistivity exhibits a sharp peak—this can be thought of as a result of the zero DOS. For $n > 0$, the charge carriers are negatively charged electrons.

ungated, or charge neutral, graphene has the Fermi level at the touching point of the conduction and valence bands. The density of states (DOS) at this point (called the Dirac point or the charge neutrality point) is 0, so the conductivity of graphene is suppressed. As the charge density is changed by gating, the conductivity increases.

1.3 Twisted bilayer graphene

Adding a twist between two layers of graphene opens a whole new realm of electronic states. The real space moiré pattern (shown in Fig. 1-4a) translates to momentum space, causing, for example, the Dirac cones to separate by $\Delta K_m \propto \sin(\theta/2)$. This separation means that the layers will be decoupled at low energies. Already from this simple decoupling we notice that now, rather than a four-fold degenerate Dirac cone, we have an eight-fold degeneracy. Moreover, as shown in Fig. 1-4c, for small twist angles, the Dirac cones hybridize at their crossing point and a van Hove singularity appears, as indicated by the black arrow in Fig. 1-4c and d. Van Hove singularities are saddle points in momentum-space where the DOS diverges and is non-differentiable

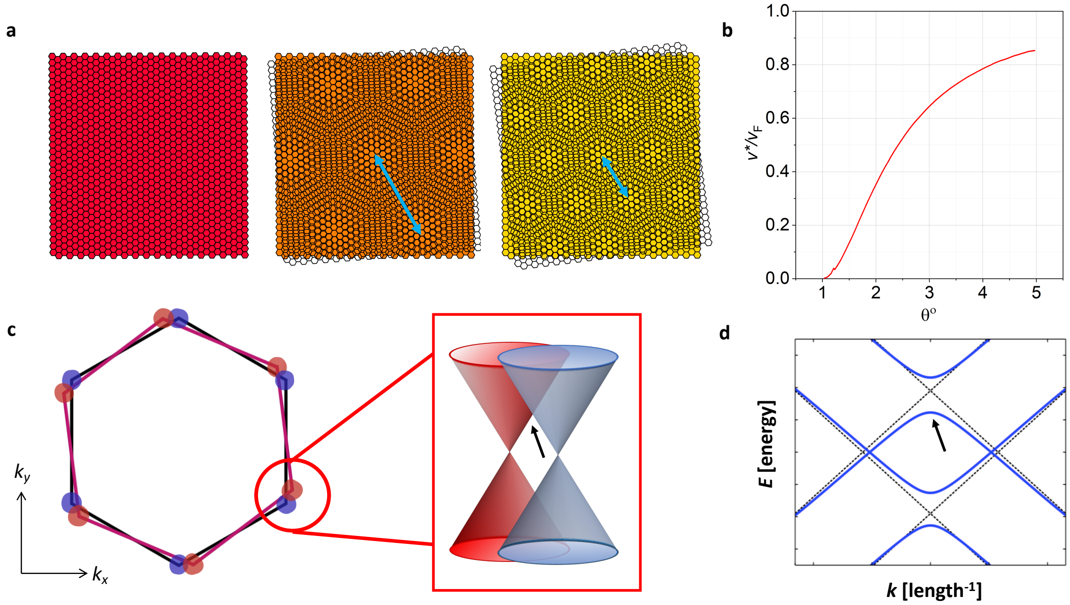

Figure 1-4: Basics of twisted bilayer graphene. **a)** A moiré pattern emerges as the twist angle is increased from 0. The blue arrows indicate the moiré lengthscale, $\lambda = a/2\sin(\theta/2)$. **b)** A low-energy continuum model of a SA-TBG system indicates that the Fermi velocity should be suppressed as the angle decreases, reaching 0 around 1.1°. Adapted from [5]. **c)** Overlapping Dirac cones in momentum space yield decoupling of the layers at low energies and van Hove singularities where the cones overlap, indicated by a black arrow. **d)** A line cut through the K points of the two lattices with a van Hove singularity indicated by a black arrow. Grey lines indicate the individual layers' Dirac cones before hybridization.

[56]. Initial theoretical calculations suggested that at small angles the layers would become more strongly coupled and the Dirac dispersion would flatten, resulting in a corresponding decrease of the Fermi velocity. For certain "magic" angles, the Fermi velocity was predicted to decrease to 0 m/s when the lowest energy bands hybridize to form flat bands, as shown in Fig. 1-4b [5]. On the other hand, at large twist angles, the two Dirac cones are completely isolated in momentum space, and the two layers are totally decoupled.

It is in the regime of small twist angle that many interesting states have been observed over the past few years, including superconductivity, ferromagnetism, and integer quantum Hall states [10, 53, 47, 45]. Despite intense theoretical and experimental interest in the topic, the regime of small twist angles is not fully understood. For this reason, we explore a number of physical properties previously explored in mono- and bilayer graphene and study the effects of twist angle on those properties.

Chapter 2

Experimental Techniques for SA-TBG Devices

2.1 The importance of high-quality devices

One of the major developments in graphene device fabrication came with the realization that the insulating crystal hexagonal boron nitride (hBN) can form an extremely clean interface with graphene, allowing for in-plane electron mobilities in excess of $10^5\,\mathrm{cm^2V^{-1}s^{-1}}$ [14, 54]. hBN has the same honeycomb structure and a very similar lattice constant to graphene, except the A and B sites are occupied by boron and nitrogen atoms instead of carbon, breaking sublattice symmetry and making hBN an insulator, with a large gap of 6 eV. Because hBN is a layered material like graphene, it can also be exfoliated down to a discrete number of layers, making it an exceptionally flat surface for graphene. Additionally, its large band gap means hBN does not interfere with electronic transport measurements of graphene and can be used as a dielectric through which to gate the graphene. Encapsulating graphene in hBN reduces charge disorder and strain and has allowed for the observation of subtle phenomena in the graphene two-dimensional electron gas (2DEG) [13, 22, 54].

However, the need for ultraclean devices did not stop simply at hBN. Although the interface between hBN and graphene is significantly cleaner than between graphene and SiO_2, the substrate commonly used before hBN, it is not perfect. Hydrocarbons are easily trapped between the layers, forming bubbles that strain the materials and locally change the electronic properties in graphene. Because transport can be thought of as a global probe, local disorder cannot be avoided, instead averaging into the overall behavior and easily obscuring finer details. Big, clean devices can be extremely valuable both for revealing delicate physics that live in the bulk by reducing the edge contributions, and for revealing in physics that requires large cyclotron orbits. Because of this, I pursued the development of “hot-ironing” and “hot-release” techniques, outlined below, that help push bubbles out from the interfaces. As an additional benefit, these techniques can also reduce twist-angle inhomogeneity [40].

I illustrate the importance of ultraclean devices by demonstrating how my devices enabled new physical phenomena to be revealed in two projects I collaborated on.

2.1.1 Doppler effect in graphene plasmons

First, inspired by theoretical work [6], we investigated the Doppler effect in graphene plasmons. In collaboration with Professor Dmitri Basov’s group at Columbia University, we used near-field infrared imaging techniques to measure the shift in plasmon frequency as a function of applied current. Similar to the optical Fizeau effect, we see that plasmons are “dragged” in the presence of a strong current flow and exhibit a Doppler shift. The challenges in this project were twofold: in order to perform near-field imaging, the top hBN must be very thin. Additionally, for plasmons to propagate as far as possible, we want a clean, bubble-free interface with low disorder. Using the “hot-release” technique previously mentioned, I was able to fabricate such devices.

2.1.2 THz-induced resistance oscillations

Second, in collaboration with Professor Sergey Ganichev’s group at the Terahertz Center, University of Regensburg, we observed resistance oscillations similar to microwave-induced resistance oscillations previously observed in GaAs quantum wells. Graphene provides an alternative 2D electron system in which to explore radiation-induced

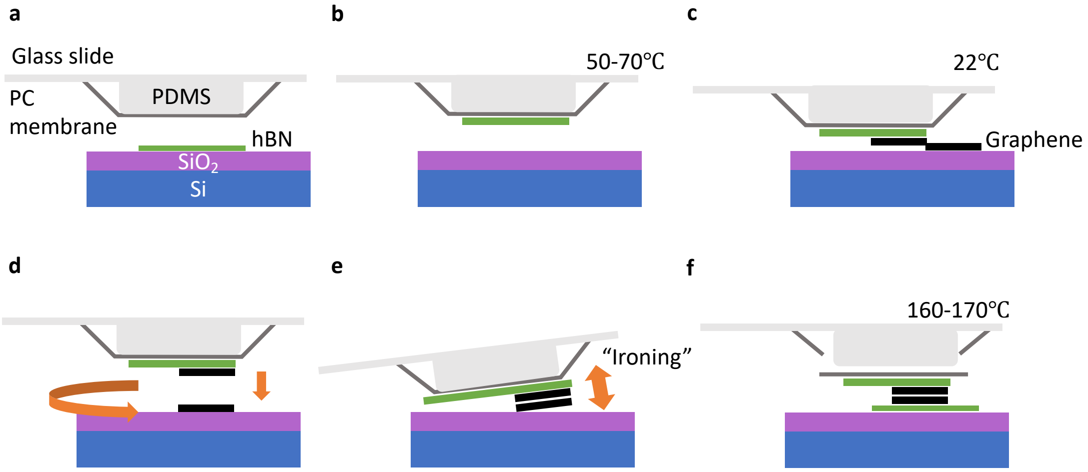

Figure 2-1: Steps of fabrication. **a)** A PC slide is mounted in a homemade transfer system. The selected hBN crystal exfoliated on Si/SiO_2 is placed in the transfer stage and heated to 50-70° C. **b)** The PC slide is lowered at an angle of 2-3°s and is used to pick up the hBN. **c)** The temperature of the stage is lowered to room temperature, and a large flake of monolayer graphene is placed on the stage. The flake may be precut by laser, or may be torn in half during the transfer process. The edge of the hBN is used to define the tearing edge. **d)** The hBN and first piece of graphene on the PC slide are raised slightly above the stage, and the stage is rotated to the target angle. The PC slide is then lowered to pick up the second piece of graphene. **e)** We perform room temperature ironing by repeatedly pressing the hBN-graphene-graphene stack against the Si/SiO_2 substrate immediately after picking up the second graphene. **f)** The stack is released onto a prefabricated and cleaned hBN-graphite stack at 160-170° C. Ironing may be performed at high temperature during this step as well.

magnetotransport. In monolayer graphene and tBLG, we found a number of interesting THz-assisted phenomena, including THz-radiation-induced magneto-oscillations. Once again, having extremely large, clean devices was imperative because several cyclotron orbits must fit within a single device at relatively low fields (and thus large radius). The "hot-ironing" technique mentioned above allowed for the fabrication of such devices.

2.2 Device fabrication techniques

All of our devices consist of hBN-encapsulated twisted bilayer graphene, which we fabricate using a modified version of the "twist–and–tear" technique [7]. We use

Scotch tape to exfoliate monolayer graphene and 30-80 nm-thick hBN on a standard Si/SiO$_2$ substrate. By adhering crystals to the tape, pressing the crystals against the substrate, and then using the tape to peel away the bulk, we are left with thin flakes on the Si/SiO$_2$ substrate. We found that heating the Si/SiO$_2$ substrate to 180 °C prior to graphene exfoliation increased the yield of large mono- and bilayers. Additionally, we anneal the exfoliated hBN crystals 350 °C for 3 hours while flowing argon and hydrogen in order to remove tape residues. We use optical microscopy to find large graphene monolayers and thin (30-70 nm) hBN crystals. Dark field microscopy can show cracks, thickness inhomogeneity, and residues that are not visible in bright field microscopy.

Then, using a homemade transfer system with μm-accuracy and a polycarbonate (PC) membrane stretched over a small (8 mm×8 mm×4 mm) polydimethylsiloxane (PDMS) polymer block on a glass slide, we assemble hBN and graphite stacks on a Si/SiO$_2$ wafer. To minimize strain on the hBN, we pick up at 50-70 °C, when the membrane is just barely sticky enough to allow for a clean pickup. The graphite is picked up at room temperature, and then the entire stack is "ironed" by repeatedly pressing the hBN-graphite stack against the Si/SiO$_2$ wafer and then released on a clean Si/SiO$_2$ wafer at high temperatures (160-170 °C [40]. We note that the ironing may be performed twice: at low temperature on the Si/SiO$_2$ onto which the graphite was exfoliated, and at 160 °C on the clean Si/SiO$_2$ wafer before release. After removing the polymer membrane with chloroform, we anneal the hBN and graphite stack at 350 °C for 3 hours while flowing argon and hydrogen in order to ensure the removal of any residues. We then assemble the hBN and twisted bilayer graphene stack using a modified version of the "tear-and-stack" method, shown in Fig. 2-1 [7]. We note that instead of tearing the graphene, we can cut the graphene in half before the transfer process begins using a continuous-wave laser —a method that we found both reduces potential issues associated with the graphene not tearing cleanly and strain-induced bubbles from the tearing process. After every step of transfer in this process, we perform low-temperature "ironing" to push out bubbles and reduce twist inhomogeneity. The three-layer stack is then released onto the previously fabricated and cleaned bottom hBN and graphite gate at roughly 160 °C. After this point, we avoid heating the stack above 180 °C to reduce the possibility twist angle relaxation. An artistic rendering of the process is shown in fig 2-1.

We then perform atomic force microscopy (AFM) on the assembled structures (Fig. 2-2c). We note that for top and bottom hBN with thickness $> 20\,\text{nm}$ that dark field optical microscopy is typically sufficient to determine the location of most bubbles (Fig. 2-2b). AFM, however, allows us to determine the location of bubbles and other irregularities precisely down to 100 nm or less. We select a clean region to serve as our device.

The encapsulated tBLG heterostructures are patterned into Hall bars using electron beam lithography (EBL). For EBL we use a double-layer polymer resist composed of polymethyl methacrylate (PMMA). The bottom layer is 495,000 molecular weight resin with 4% solids in anisole spun to 2000 Å and baked at 180° C for 7 minutes. The top layer is 950,000 molecular weight resin with 2% solids in anisole spun to 750 Å and baked at 180° C for 3 minutes. The polymer resist is systematically patterned by the electron beam. The double-layer creates an undercut during electron beam lithography (EBL), allowing for better lift-off (see below).

We use an Elionix EBL system to perform EBL with resolution of a few nanometers. For large features, we use a resolution of 10 nm and a dose of $2000\,\mu\text{C/cm}^2$ at 20 nA beam current. For finer features, we use a resolution of 2.5 nm and a dose of $2600\,\mu\text{C/cm}^2$ at 2 nA beam current. For the final etching in which we remove all surrounding hBN and graphene except that between the contacts —also known as the final mask— we use a resolution of 2.5 nm and a dose of $1200\ \mu\text{C/cm}^2$ to prevent accidental overexposure of smaller features. We perform cold development using 1:3 isopropyl alcohol:water at 0 °C for 60 s, resulting in the pattern shown in Fig. 2-2d.

Etching of hBN and graphene is performed using reactive ion etching (RIE) on an Inductively Coupled Plasma etching system (STS). We first perform a light O_2 plasma cleaning to remove PMMA residues that were not reduced during development. Then, using plasma generated by a mixture of Ar, CHF_3, and O_2 gases, we selectively etch away the hBN in the parts of the heterostructure unprotected by the lithographic mask (Fig. 2-2e). With this recipe, typical etching times for hBN are on the order of 5 nm per second. Graphene etches much more slowly, on the order of 20 seconds for monolayer graphene.

Metal is evaporated into contacts via thermal evaporation using a Sharon Thermal Evaporator at $< 1\mathrm{e}{-6}$ Torr. For contacts, 3 nm chromium is deposited as a sticking layer via thermal evaporation [52]. Then 50-70 nm of gold, depending on the thickness of the hBN-graphene heterostructure, is deposited on top of chromium.

Liftoff —the removal of PMMA resist and any residual metal from thermal evaporation— is performed by completely submerging the device in acetone at room temperature for between 4-12 hours. While submerged, a plastic pipette can be used to flush the device with acetone to accelerate liftoff. The final result is shown in Fig. 2-2f.

We repeat the same EBL and thermal evaporation procedures to define a metallic top gate (3 nm chromium and 30-40 nm gold). Finally, we repeat the same EBL and etching procedures to define the final Hall bar geometry, using for RIE, in this case, a plasma generated by only O2 and CHF_3 gases (Fig. 2-2g).

After the device is completed, we wire-bond the device onto a chip carrier specifically selected for our measurement system, as shown in Fig. 2-2h.

2.3 Measurement methods

All of the data shown was taken in either a home-built He-4, 4K probe setup or in a Janis He-3 system (Fig. 2-3a). We use a Lakeshore 340 Temperature Controller to control the temperature between 300 mK and room temperature. The magnet in both systems is composed of superconducting copper wire and is controlled by a Cryomagnetics Helium Monitor and a Agilent Triple Output Power Supply. We perform measurements using Stanford Research Systems (SRS) SR830 lock-in preamplifiers, SR560 voltage preamplifiers, and Keithley 2400 Sourcemeters. In the 4K setup, a single vacuum pump controls the sample chamber. In the He-3, two turbo pumps control the sample chamber and the 1K pot separately.

All of our measurements are taken in devices with a Hall bar configuration. We

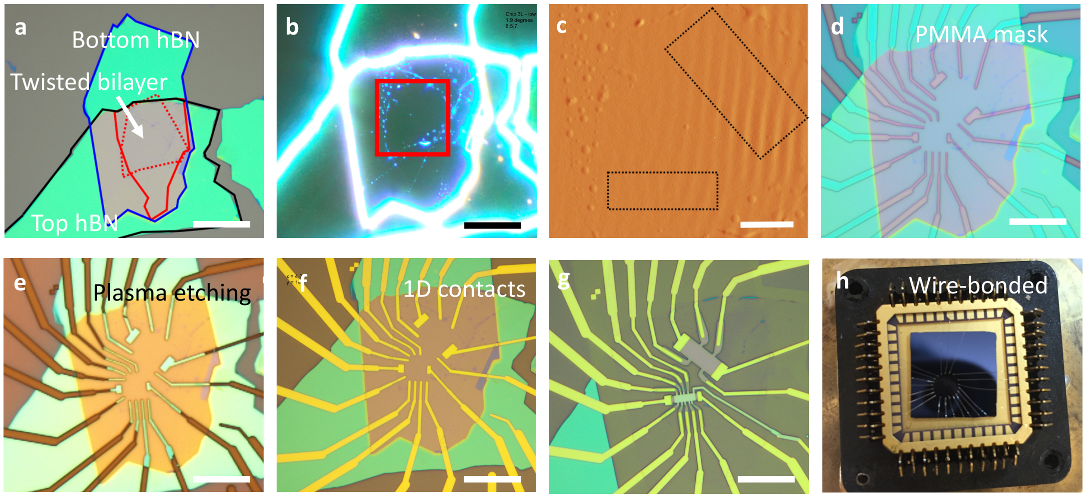
a
Bottom hBN
Twisted bilayer
Top hBN
b
c
d
PMMA mask
e
Plasma etching
f
1D contacts
g
h
Wire-bonded

Figure 2-2: Images at various steps of fabrication for TBG-2.3°. **a)** Encapsulated twisted bilayer graphene. Bottom hBN (blue), top hBN (black), and twisted bilayer (red) after PC removal on a high-conductivity Si/SiO_2 substrate. Scale bar: 30μm. **b)** Dark field image of heterostructure with region examined via atomic force microscopy (AFM) indicated in red. Scale bar: 20μm. **c)** AFM image of regions used for Hall bar. Ripples are an artifact of the AFM and are not physical. White bar is 5 μm. **d)** Protective PMMA mask. Scale bar: 18μm. **e)** Contact regions after plasma etching. Si/SiO_2 substrate appears brown. Scale bar: 20μm. **f)** Contact regions after metal deposition and lift-off. Scale bar: 20μm. **g)** Hall bar after top gate is added and final etching. Scale bar: 15μm. h) Device bonded to ceramic chip carrier (gold-colored region: 2cm×2cm).

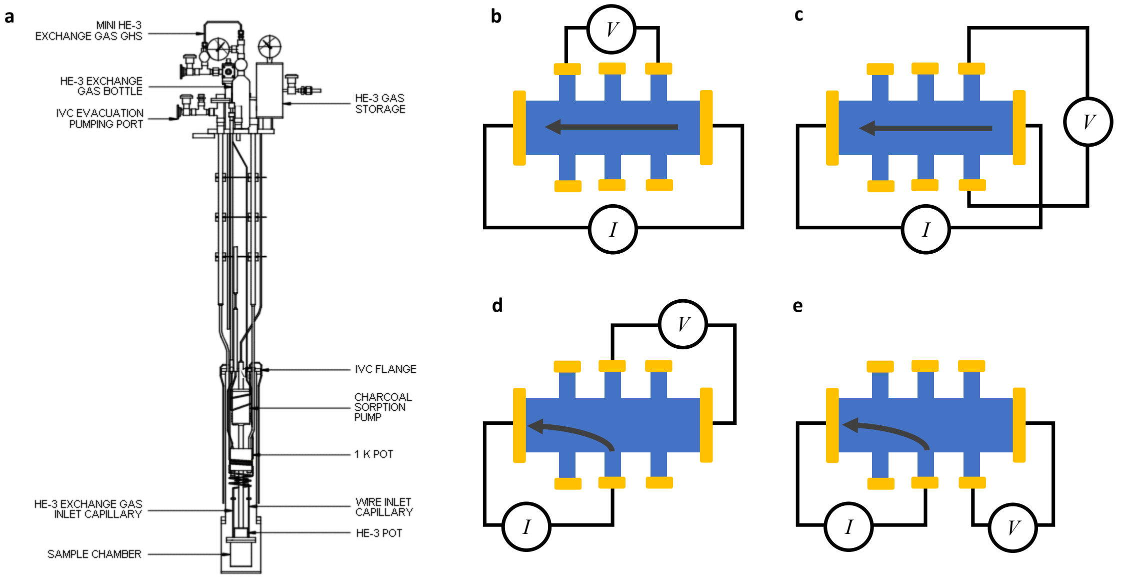
a
MINI HE-3 EXCHANGE GAS GHS
HE-3 EXCHANGE GAS BOTTLE
IVC EVACUATION PUMPING PORT
HE-3 GAS STORAGE
IVC FLANGE
CHARCOAL SORPTION PUMP
1 K POT
HE-3 EXCHANGE GAS INLET CAPILLARY
WIRE INLET CAPILLARY
HE-3 POT
SAMPLE CHAMBER
b
V
I
c
V
I
d
V
I
e
I
V

Figure 2-3: Measurement system. **a)** A Janis He-3 system with exchange gas. Our fridge is an older version of the diagram shown. Diagram from Janis Research. **b)** Four-terminal measurement configuration for determining the resistance of the channel. **c)** Hall effect measurement configuration. Magnetic field points out of plane. **d)** Bend resistance measurement configuration for measuring ballistic transport. **e)** Transverse magnetic focusing and vicinity resistance measurement configuration for studying ballistic transport and viscous flow, respectively.

show the device configurations referenced in the later sections in Fig. 2-3b-e.

2.3.1 Device characterization

Characterizing and understanding the device is a crucial part of the experimental process. Here we describe the primary characterization measurement configurations and explain their implications.

Longitudinal resistivity

As mentioned previously, graphene has linear energy dispersion that crosses through a zero DOS point called the Dirac point. Charge inhomogeneity will cause a broadening of this point with a width roughly corresponding to the size of the charge puddles. In order to get a sense of the magnitude of this broadening, we drive an AC current, I, through the sample between two contacts (source and drain) and measure the voltage drop, V_{xx}, between two others along the direction of current, while simultaneously sweeping the gate, V_G, from negative to positive voltage, thereby changing the carrier density and moving the Fermi level from the valence to the conduction band (Fig. 2-3b). We calculate the sheet resistance as $\rho_{xx} = (V_{xx}/I)(L/W)^{-1}$, where L is the distance between the contacts and W is the width of the Hall bar. From the resistivity, we can also calculate the mobility, $\mu = (\rho_{xx} n e)^{-1}$, where n is the carrier density. Modeling the gate-hBN-graphene as a capacitor, the carrier density is proportional the gate voltage, $n \propto cV$, where c is the capacitance of hBN per area. When the Fermi level is in the valence band, graphene behaves as a metal where the charge carriers are holes, and the resistance is very small —typically a few Ω at $4\,\mathrm{K}$. As the Fermi level reaches the Dirac point, the number of available states goes to 0, meaning that the resistance spikes, typically to one or two kΩ. Moving the Fermi level into the conduction band allows graphene to behave as a metal once again with electrons as the charge carriers, therefore the resistance once again drops to a few Ω. We are left with a characteristic curve of carrier density versus resistivity (Fig. 2-4a).

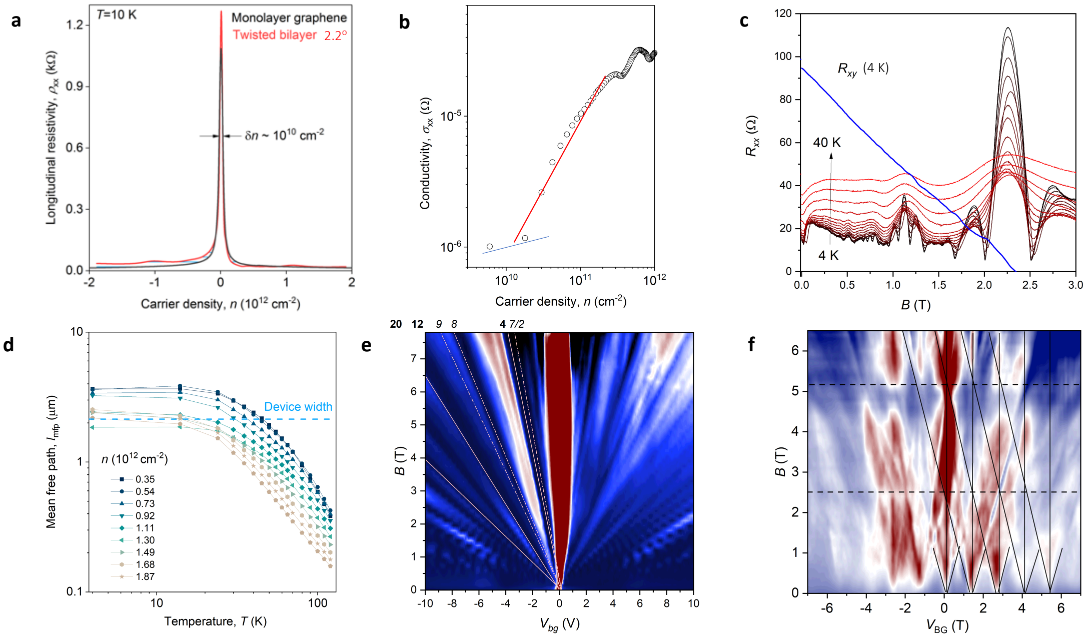

Figure 2-4: Standard characterization measurements for TBG-2.2°. **a)** Comparison between the Dirac peak of TBG-2.2° and of monolayer graphene. Both are similarly narrow with a charge inhomogeneity on the order of $\delta n = 10^{10}\text{cm}^{-}2$. This is a low charge inhomogeneity, likely due to the fact TBG-2.2° uses a graphite gate. **b)** Conductivity versus carrier density for electrons, plotted on a log-log scale. Where the red and blue lines intersect indicates δn, which matches with the width of the Dirac peak in a). **c)** Longitudinal (R_{xx}) resistance, plotted as a function of out-of-plane magnetic field and temperature (black to red). The low temperature oscillations are Shubnikov de Haas oscillations, which are suppressed as temperature is increased. Lower frequency magnetophonon oscillations become clearly visible at these higher temperatures. The Hall (R_{xy}) resistance at 4 K is plotted in blue on top. At higher magnetic fields, plateaus are visible in R_{xy}, corresponding to the filling of Landau levels. **d)** Mean free path for electrons, l_{mfp}, versus temperature T, calculated at a range of carrier densities, n, in TBG-2.2°. l_{mfp} is larger than or comparable to the device width up to 20 K for all carrier densities, demonstrating exceptional ballistic transport. **e)** Landau fan with fits to various filling factors plotted in pink. The Landau fan filling factor sequence for TBG will be (8N+4), double that of monolayer graphene. As a side note, magic angle TBG will have (4N+4). **f)** Landau fan for TBG-0.5°. A beautiful Hofstadter butterly pattern is visible, where we have added black lines to guide the eye. More experimental data is required to determine the exact angle of this device.

The Hall effect and the quantum Hall effect

The Hall effect also gives us a sense of the device's behavior (Fig. 2-3c). Current is driven in the channel and the voltage drop across the channel, transverse to current, V_{xy}, is measured in the presence of an out-of-plane magnetic field. The classical Hall effect tells us that a voltage difference will be produced transverse to the magnetic field and current. In a 2DEG, the carrier density is related to the transverse, or Hall, resistivity by $\rho_{xy} = B/ne$, thus we can use the Hall effect as one way of determining the capacitance of the hBN dielectric by measuring ρ_{xy} as a function of gate voltage at fixed magnetic field. Besides the Hall effect, we can also observe cyclotron motion, characterized by the cyclotron frequency, $\omega_c = eB/m_c$.

At strong enough electric fields, such that $\omega_c \tau \sim 1$, where τ is the electron scattering time, the classical Hall effect picture fails. We see this as oscillations in ρ_{xx}. This behavior is fundamentally due to the DOS of the 2D electron gas (2DEG). Under the application of a magnetic field, a general 2DEG DOS becomes a sequence of evenly spaced peaks called Landau levels (LL) [19]:

$$N(E, B) = \frac{geB}{h} \sum \delta\left(E - E_n\right) \tag{2.1}$$

where g is the degeneracy of the 2DEG ($g = 4$ for monolayer graphene, $g = 8$ for TBG). For a simple harmonic oscillator, $E_n = \hbar\omega_c(n+\frac{1}{2})$ with $n = ..., -2, -1, 0, 1, 2, ...$, so we have evenly spaced LL. In the case of the graphene 2DEG, however, because of the Dirac dispersion, the LL are not evenly spaced. Solving the Schrodinger equation for a massless Dirac fermion, we get the relation:

$$E_n = \mathrm{sgn}(n)\sqrt{2e\hbar v_F^2 |n| B} \tag{2.2}$$

We note that, in reality, the peaks in the DOS are broadened by disorder proportional to $1/\tau$. These peaks give rise to the oscillations in ρ_{xx} that we observe, typically called Shubnikov de Haas oscillations (SdHO) [19]. Each LL has geB/h available states, therefore the oscillations are periodic in $1/B$, corresponding to the filling of

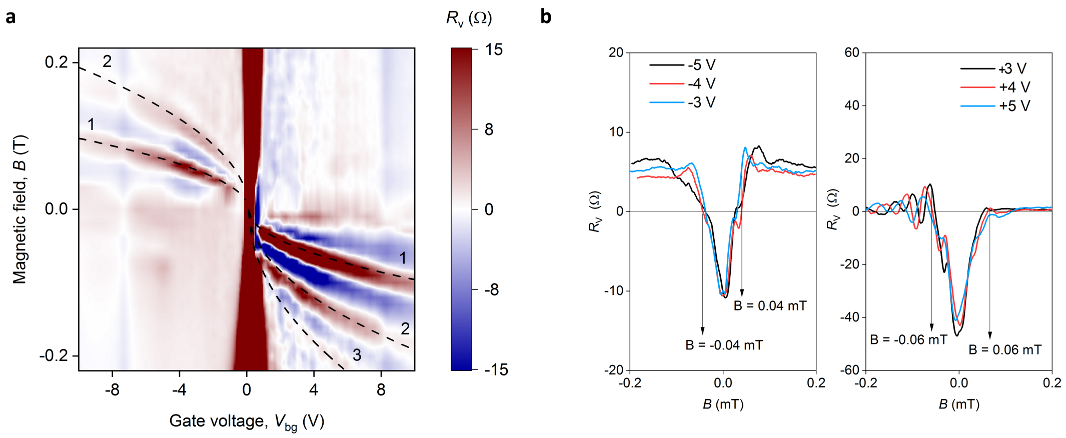

Figure 2-5: Data from ballistic characterization of SA-TBG devices. **a)** Transverse magnetic focusing for TBG-2.2°. Fits to equation 2.3 are plotted and show good agreement with the eight-fold degeneracy of TBG. **b)** Bend resistance for TBG-2.2°.

each LL. We can use these oscillations to determine the cyclotron mass, as explained in the next section.

At high enough magnetic field, the oscillations in ρ_{xx} become peaks with vanishing resistivity in between. ρ_{xy} becomes quantized in integer multiples of the universal constant h/e^2. This regime is called the quantum Hall regime. These effects can all be observed using the measurement configuration in Fig. 2-3b.

Ballistic characterization

In order to make sure our devices are of high-quality, we want to observe long-distance ballistic transport at low temperatures. We perform two main characterizations: transverse magnetic focusing and bend resistance measurements.

Transverse magnetic focusing measures the drop in voltage at a specific distance from an injection point as electrons are bent along cyclotron orbits as shown in Fig. 2-3e [50]. The magnetic field required to bend an electron in a half orbit from an injection point a distance L to the measurement point is

$$B = \frac{2\hbar k_F}{eL} \tag{2.3}$$

where in TBG, $k_F = \sqrt{\frac{\pi n}{2}}$, yielding $B \propto \sqrt{V_{\text{gate}}}$. When Eq. 2.3 is satisfied, we see a positive resonance in voltage versus magnetic field. We show an example of such data in Fig. 2-5a.

Bend resistance provides a measure of the tendency of ballistic electrons to "overshoot". As shown in Fig. 2-3d, a negative resistance measured directly across a Hall bar channel from the drain indicates "overshooting" behavior and signifies ballistic transport. An example of data is shown in Fig. 2-5b.

2.3.2 Determining twist angle

Although we aim for a particular angle during the fabrication process, the final device is rarely at the targeted angle. The hot release technique as well as all other steps in the fabrication process (including baking the PMMA resist) strain and heat the device repeatedly, which can cause random relaxation of the angle. Therefore, it is extremely important for us to determine the twist angle via transport measurements after the device is completed and cooled. We outline three ways that we use to determine twist angle but note that there are several other methods as well.

Cyclotron mass

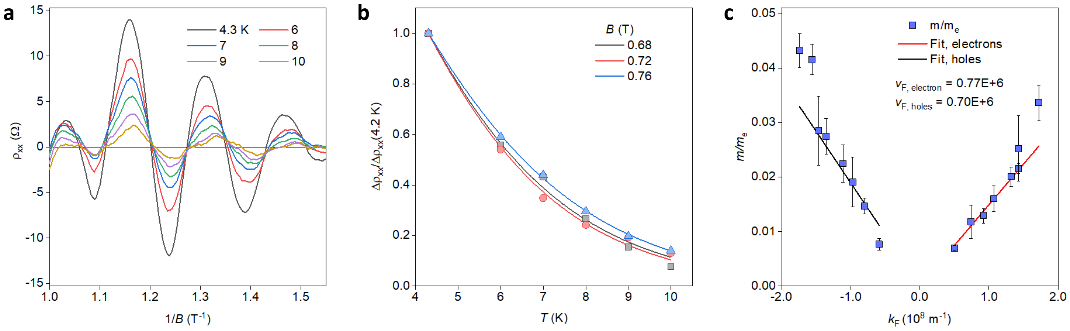

Figure 2-6: Fitting cyclotron mass with the Lifshitz-Kosevich formula for TBG-2.2°. **a)** Quantum oscillations at various temperatures with polynomial background removed. **b)** Normalized amplitudes versus temperature, fitted to Eq. 2.6 for three different values of B. **c)** m_c versus k_F, fitted assuming Dirac spectrum to find the Fermi velocity. Error bars are calculated as described in the main text.

As previously mentioned, we expect the Fermi velocity to be suppressed in twisted bilayer graphene, as in Fig. 1-4b. We can calculate the Fermi velocity and then use theoretical predictions to determine the angle based on how much the Fermi velocity has been suppressed. Assuming a Dirac spectrum, the Fermi velocity is given by

$$v_F = \frac{k_F}{m_c} = \frac{\sqrt{\pi n/2}}{m_c} \tag{2.4}$$

where we obtain the right side of the equation from Eq. 2.2. Therefore, we just need to determine m_c at fixed n to get v_F. Note that because we assume a Dirac spectrum, this method works for small n only.

We determine the cyclotron mass m_c versus carrier density n by fitting SdHO as a function of temperature using the Lifshitz-Kosevich formula [39]:

$$\rho = e^{-D}\lambda(T)/\sinh\lambda(T)\cos(2\pi\frac{B_F}{B} + \pi + \phi) \tag{2.5}$$

where $\lambda(T) = 2\pi^2 k_B T m_c/\hbar e B$, D is the Dingle factor contribution, and B_F is the fundamental frequency. We work in a range of temperatures from 4 K to 10 K where we find the quantum oscillations are strongest. We first subtract off any background oscillations by subtracting $\rho_{xx}(20\,\mathrm{K})$ from $\rho_{xx}(T)$. To further isolate the quantum oscillations, we subtract off a second-order polynomial background, resulting in the curves like those shown in Fig. 2-6a.

For a given carrier density, we extract the amplitude of ρ_{xx} as a function of temperature and magnetic field. We then normalise to the amplitude at 4 K in order to remove the Dingle factor, allowing us to fit the normalized amplitude versus temperature to the following simplified formula:

$$\Delta\rho_{xx}(T)/\Delta\rho_{xx}(T_0) = \lambda(T)\sinh\lambda(T_0)/\lambda(T_0)\sinh\lambda(T) \tag{2.6}$$

and extract m_c, which we plot in Fig. 2-6b. The error from the fit contributes an error of 1 to 10% and the error in the fit at various B contributes a standard deviation error of about 10%. We then plot m_c versus k_F, and, assuming a linear dispersion, derive the Fermi velocity as in Fig. 2-6c.

Fitting in the presence of multiple types of QO

Special thanks to Clément Collignon for providing a great deal of guidance in this section.

The method of analysis described above works well when the only oscillations present are SdHO. However, if another type of oscillation is present under the same conditions as SdHO, we will experience a beating of the two. Worse, if the second oscillation has a different temperature or carrier density dependence, we will potentially pick up this modulation in the fit, giving an inaccurate estimate of the effective mass. Assuming that the second type of oscillation has a difference frequency, we can use a fast Fourier Transform (FFT) to separate out the two oscillations and their respective temperature dependences.

We first take the second derivative of ρ_{xx} with respect to B, which removes an additive background of up to second order (Fig. 2-7b). We then perform FFT on $\partial^2\rho_{xx}/\partial B^2(1/B)$ using a Blackman window centered on a hand-picked region with the cleanest oscillations (Fig. 2-7c). An additional trick we may play in order to improve the FFT sampling is to set ρ_{xx} to 0 outside the Blackman window for a wide range of $1/B$. We then take a linecut through the maxima at the fundamental frequency B_F, and fit it to the Lifshitz-Kosevich formula in Fourier space following Eq. 2.5 (noting the cosine term simply gives us the peak at B_F). We perform the fitting with two variables, m and e^{-D}, the latter of which we simply set to a fixed amplitude, and we set B to be the center of the Blackman window.

We then repeat this process for a few sets of Blackman windows with different centers to make sure the fundamental frequency is independent of our choice of region (Fig. 2-7d).

This method also allows us to access both the Dingle factor D and the secondary oscillation's temperature dependence, which will appear as a second peak (which we must be careful to differentiate from the harmonics of B_F).

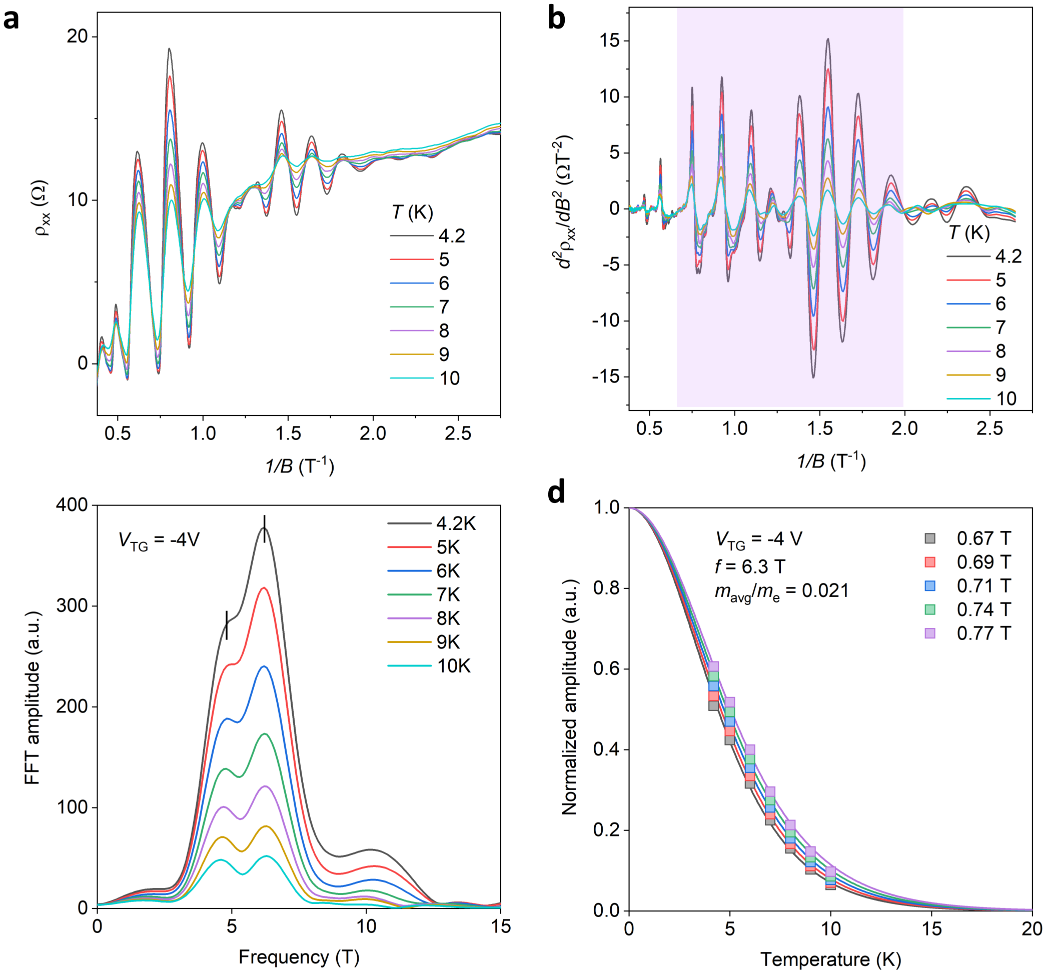

Figure 2-7: Determining effective mass using FFT analysis for TBG-2.3° at $-4\,\mathrm{V}$ on the top gate. **a)** Raw resistivity data versus 1/B. **b)** Second derivative of data in **a)** to remove up to second order polynomial background. The purple indicates the region we select by hand to perform FFT on. **c)** FFT of purple region in **b)** with a Blackman window applied. The true B_F is the dip between the two peaks indicated. The double peak (black vertical lines) is a result of beating between SdHO and magnetophonons. **d)** We perform **b)** and **c)** four times, each time moving the purple window slightly to the left and right to double check that the effective mass and fundamental frequency do not shift with the choice of window. We fit the four windows and average to find the effective mass, $1.91 \times 10^{-32}\,\mathrm{kg}$.

Filling of the lowest superlattice band

The previous method of determining twist angle by suppression of Fermi velocity relies heavily on theoretical predictions for the functional dependence of Fermi velocity on angle. Much still remains to be understood about twisted bilayer graphene, so we cannot wholly trust these calculations. Therefore, a more accurate way to determine the angle relies on determining the carrier density at which the superlattice gaps appear, i.e. the density required to fill one band in the superlattice. This carrier density is defined as

$$n_s = \frac{4}{A} = 4 \times \frac{8\sin^2(\theta/2)}{\sqrt{3}a^2} \tag{2.7}$$

where A is the area of the moiré unit cell and a is the graphene lattice constant, 2.46Å. We can approximate the right side of 2.7 as $\approx \frac{8\theta^2}{\sqrt{3}a^2}$.

The filling of one superlattice band, therefore reaching the superlattice gap, will appear as a huge increase in resistance in transport. Additionally, at roughly $n_s/2$, we will see the sign of the Hall resistance change at the van Hove singularities.

A few caveats for this method exist: for small twist angles, localized states make it difficult to determine n_s accurately. Additionally, for twist angles below ≈ 1°, Ref. [9] and others have experimentally observed that the resistance peaks in transport data may correspond to $2n_s$ rather than n_s, giving an ambiguous factor of $\sqrt{2}$ in the angle.

Brown-Zak oscillations

The final and perhaps most accurate way to determine twist angle is through Brown-Zak oscillations (BZO) [3]. BZO occur when there is a superlattice due to spatial quantization on the length scale $L \approx aq$, where q is the number of units cells in the miniband.

We can use the relation between angle and size of the superlattice unit cell area to find the relation

$$\frac{\sqrt{3}a^2}{2\theta^2} = \Delta(\frac{1}{B})\phi_0 \tag{2.8}$$

where $\Delta(\frac{1}{B})$ is the period of BZO versus $1/B$ and ϕ_0 is the magnetic flux quantum.

BZO do not appear in all our samples, and so, although this method is the most

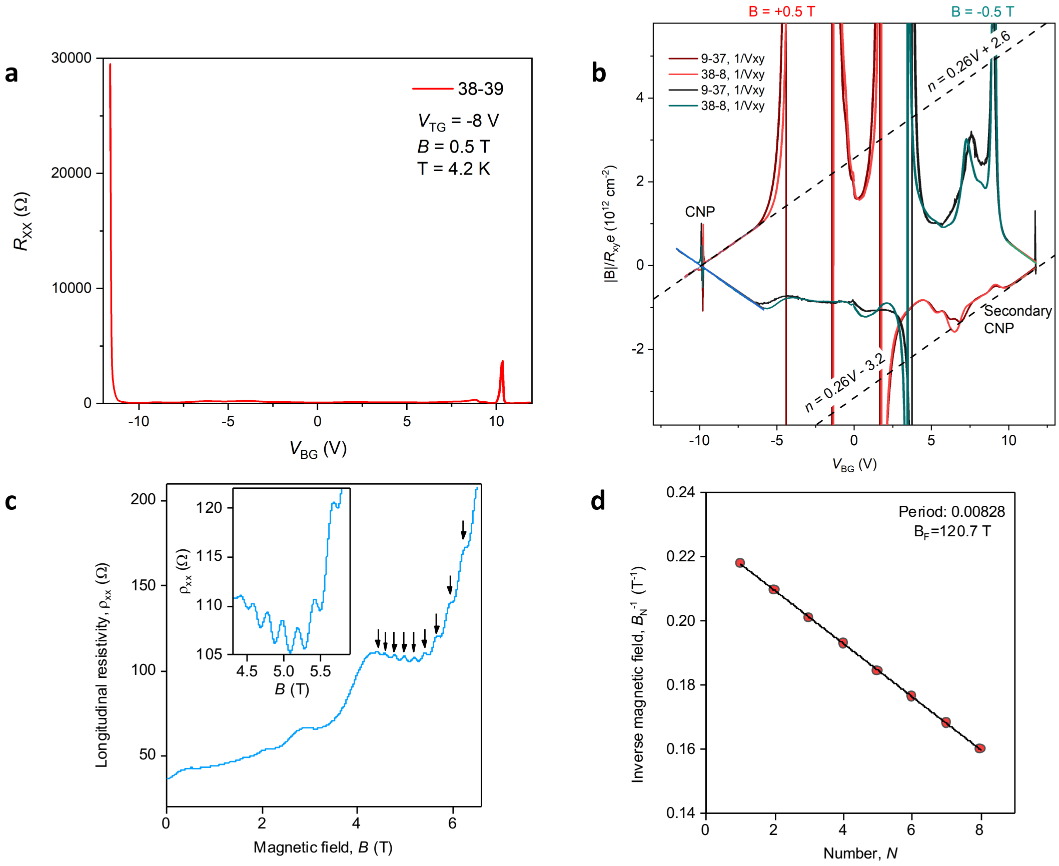

Figure 2-8: Alternate methods of determining twist angle. **a)** Longitudinal resistance versus backgate voltage (directly proportional to carrier density). The Dirac peak appears as a small peak on the right, and the superlattice gap appears as a tall peak on the left. **b)** $1/R_{xy}$ versus backgate voltage. The superlattice gap appears as a change in sign of $1/R_{xy}$. The slope of $1/R_{xy}$ near the two neutrality points can be used to determine the capacitance of the bottom hBN, as shown by the dashed lines. **c)** Brown-zak oscillaions (BZO) versus B-field. Black arrows indicate the peaks. Note the oscillations are periodic in $1/B$. **d)** Fit of the $1/B$ locations of the BZO peaks versus peak number. The slope gives the fundamental frequency.

accurate, we have to rely on the two previous methods as well.

Now that we have the tools to first fabricate and then characterize devices, we will move on to trying to observe some interesting phenomena.

Chapter 3

Onset of Fluidity in TBG

Vicinity resistance has been shown, experimentally and theoretically, to be a simple transport probe for viscous fluid behavior in graphene systems. We show that SA-TBG devices above the magic angle display negative vicinity resistance, indicating the onset of fluidity. Furthermore, we find evidence of competition between momentum-conserving and momentum-non-conserving interactions in the same device.

3.1 Introduction - the graphene electron fluid and transport probes

Transport in many-particle systems where carrier-carrier collisions are the dominant interaction —for example, in most liquids— has been studied for over two centuries and can be accurately described by hydrodynamic theory [30]. Theoretical proposals have postulated that the collective behavior of charge carriers in solids can also be treated by the hydrodynamic approach, but experimental evidence of hydrodynamic electron transport proved difficult to find [21, 12].

However, in recent years, graphene on hBN has been shown to provide a uniquely suitable platform for the study of hydrodynamics [1, 23, 28, 49]. Advances in fabrication allow for ultraclean graphene samples with low disorder. Additionally, graphene

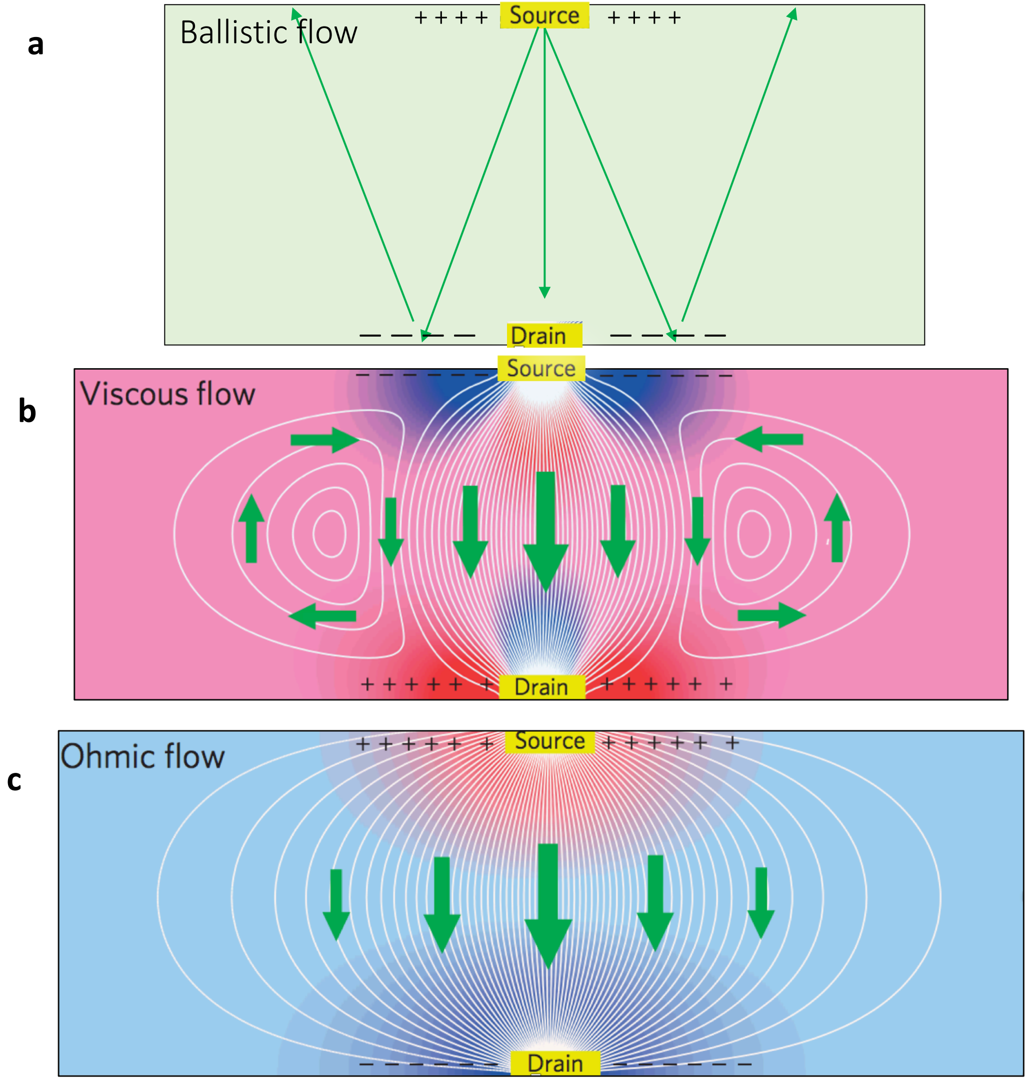
a
Ballistic flow
+ + + +
Source
+ + + +
Drain
b
Viscous flow
Source
Drain
c
Ohmic flow
Source
Drain

Figure 3-1: Visualization of the three regimes of electronic transport in a vicinity resistance measurement configuration. **a)** In the ballistic regime, vicinity resistance is positive. **b)** Shear flow in the viscous electron fluid generates an electric field opposite to the direction of the applied electric field, and vicinity resistance is negative. **c)** Vicinity resistance is once again positive in the ohmic regime. **b)** and **c)** adapted from [33]

has weak electron-phonon coupling, meaning that the electron mean free path, l_{mfp}, can be micrometers in length (larger than the system size), even up to room temperature [50]. Moreover, in an idealized graphene device, the electron-electron scattering length $l_{ee} \ll l_{mfp}$ for a range of easily accessible temperatures, meaning that carrier-carrier collisions are the dominant interaction.

So far, the behavior of electron fluids has primarily been theoretically discussed deep in the hydrodynamic regime, where l_{ee}, tunable by temperature and charge density, is the shortest length-scale of the system [33, 51]. In contrast, in graphene, experimental conditions are such that l_{ee} is comparable or at most a few times smaller than the system dimensions, allowing investigation only close to the onset of fluidity [2]. Therefore, there remains an important yet challenging task to push farther into the hydrodynamic regime in graphene where a variety of interesting phenomena remain to be explored.

It is here that twist angle provides us a third knob, other than temperature and charge density, with which to control the onset of the hydrodynamic regime. Theoretical proposals have suggested that TBG near the magic angle may exhibit enhanced hydrodynamic behavior [58]. Following this suggestion, we proposed to study hydrodynamics in the regime of SA-TBG.

3.2 Background - regimes of electronic transport

Seeing hydrodynamics at play in the macroscopic world is not too hard: properties like viscosity are tangible (watch honey slowly drip from a spoon), and physical laws like Poiseuille flow can be visualized at home (squeeze some toothpaste out of a tube). But when we pan down to the nanoscale, deciding if something can be described by hydrodynamics becomes much harder. For example, under some conditions, the electrons in graphene behave as a viscous electron fluid and therefore should theoretically obey Poiseuille's law, but visualizing this is difficult. Recently, a group managed to do this with a scanning carbon nanotube single-electron transistor, a great feat of engineering [49]. Other groups have used nitrogen-vacancy centers in diamond as quantum magnetometers to image the viscous flow of graphene and the characteristic Poiseuille parabola [23, 28]. All these methods require extremely complicated, expensive, and delicate equipment. If we could have a way quantify hydrodynamic behavior in electron transport instead, this would be an attractive alternative.

We will begin by a brief overview of the three main regimes of electron transport: the ballistic regime, the diffusive regime, and the hydrodynamic regime. The first two have been studied in solid state physics for the past 100 years or more, but the latter has only relatively recently become accessible to experimentalists. Our discussion will focus on these regimes specifically in graphene.

3.2.1 Diffusive regime and the Drude model

The diffusive regime considers electron transport on length scales much longer than the electron mean free path —the average distance an electron travels before elastically scattering off impurities. The ideas of the Drude model, which describes electrons in a metal bouncing off of heavier, immobile ions, can be applied here [24].

We can derive the conductivity by considering what happens in the presence of a weak electric field [24]. Assume the average time between collisions is τ. The average momentum of a given electron just before a collision is then $\langle \mathbf{p} \rangle = e\mathbf{E}\tau$, where e is the electron charge and $\mathbf{E}$ is the applied field. We also have that $\langle \mathbf{p} \rangle = m\langle \mathbf{v} \rangle$ and $\mathbf{J} = ne\langle \mathbf{v} \rangle$, where $\mathbf{J}$ is the current density and n is the carrier density. Combining these together, we get

$$\mathbf{J} = \sigma\mathbf{E} = \left(\frac{ne^2\tau}{m}\right)\mathbf{E} \tag{3.1}$$

From this, we can also write the mean free path $l_{mfp} = v_F\tau$, and using Eq. 3.1, can find l_{mfp} by measuring the conductivity (a simple quantity to measure in transport). Similarly, we can write the mobility, $\mu = \frac{\sigma}{ne}$. We note that at high temperatures, μ is limited by inelastic electron-phonon scattering. Such scattering process do not conserve electron momentum.

3.2.2 Ballistic regime

The ballistic regime, as its name implies, describes a regime in which electrons behave like "billiard balls" (obeying Newton's second law), with mean free path longer than the size of the system. In this regime, momentum relaxation does not occur in the bulk because scattering processes are rare, but rather occurs at the edges of the system.

As described in chapter 2, in the ballistic regime, we can observe bend resistance and magnetic focusing, both of which can be described using classical equations for an electron in a magnetic field in this regime.

3.2.3 Viscous regime and vicinity resistance

The hydrodynamic regime, as mentioned in the introduction, requires that the electron-electron scattering dominate over all other scattering processes [21, 33]. In this case, we look at the dynamics of this system on length scales and timescales much larger than the electron-electron interaction length and timescale, i.e. we consider macroscopic behavior at equilibrium rather than the behavior of individual electrons as we did in the ballistic regime. Note that, unlike the electron-phonon scattering process mentioned previously, these interactions are conserve electron momentum, a fact which is important for the formulation of hydrodynamic theory.

We can use Fermi liquid theory, which describes interacting fermions, to derive a few constants that we will later find useful. The electron-electron mean free path can be written as

$$l_{ee} = v_F \tau_{ee} \tag{3.2}$$

where v_F is the Fermi velocity and $1/\tau_{ee}$ is the electron-electron scattering rate, with

$$\tau_{ee} \approx \frac{\hbar E_F}{(k_B T)^2} \tag{3.3}$$

The physical implications of Eqs. 3.2 and 3.3 are the following: taking the limit as $T \to 0$, we see that the scattering rate $1/\tau_{ee} \propto T^2$ goes to 0 to first approximation.

After scattering, the quasiparticles go into unoccupied states, but the probability of having such an available state goes to 0. This is because the width of the Fermi surface smearing defines the probability of finding such a state, and this width is proportional to temperature as well.

How do we use transport to quantify hydrodynamic behavior? In the graphene 2DEG in particular, we can think of hydrodynamic behavior as arising from momentum conservation. Momentum is rapidly exchanged via carrier collisions in a viscous system, leading to collective behavior. Since momentum must be conserved, this collective behavior may be summarized as hydrodynamic momentum transport modes [33]. In the configuration shown in Fig. 3-1, where we drive current from source to drain by applying an electric field, momentum diffuses transverse to the direction of the applied field. This diffusion creates the shear flow and corresponding backflow, leading to "pockets" of electric field acting in the opposite direction of the applied field near the source and drain. We can also think of this as the injected current dragging the fluid adjacent to the injection point, creating negative potential regions. We can measure these "pockets" as negative nonlocal resistance, which we call vicinity resistance. In the past few years, several papers have shown that negative vicinity resistance is a reliable way to study hydrodynamic behavior in mono- and bilayer graphene devices [1, 2, 4, 26]. We will use vicinity resistance to quantify hydrodynamic behavior in SA-TBG devices [33].

3.3 Results

We fabricated two multi-terminal Hall bars consisting of SA-TBG encapsulated in relatively thick ($> 40\,\mathrm{nm}$) hBN crystals, following the methods detailed previously (p. 31). We label the devices TBG-2.2° and TBG-2.3°, referencing the twist angle. TBG-2.2° has a local graphite backgate and no topgate (Fig. 3-2a). TBG-2.3° is gated below globally by the Si wafer through $\mathrm{SiO_2}$ and locally gated above by PdAu (Fig. 3-2d). For TBG-2.3°, we determined the twist angle by Brown-Zak oscillations. In TBG-2.2°, we did not observe either of these phenomena, and so used the suppression of

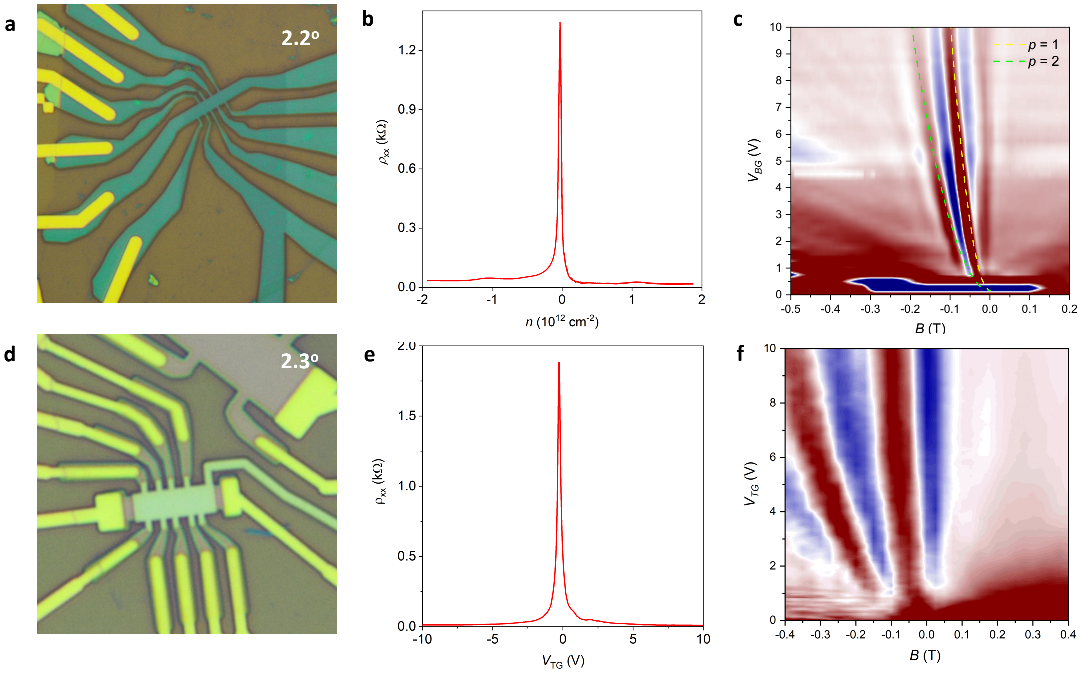

Figure 3-2: Characterization of TBG-2.2° and TBG-2.3°. Optical image of TBG-2.2°. **b)** Narrow Dirac peak for TBG-2.2°, indicating low charge inhomogeneity. The peak is narrower in carrier density than TBG-2.3°, most likely due to the fact that TBG-2.2° has a graphite backgate and TBG-2.3° has a PdAu topgate and Si bottom gate. Graphite has been shown to have lower charge disorder than metals and silicon. **c)** TMF for TBG-2.2°, showing ballistic transport over long distances. **d)** Optical image of TBG-2.3°. **e)** Narrow Dirac peak for TBG-2.3°. **f)** TMF for TBG-2.3°, showing ballistic transport over long distances.

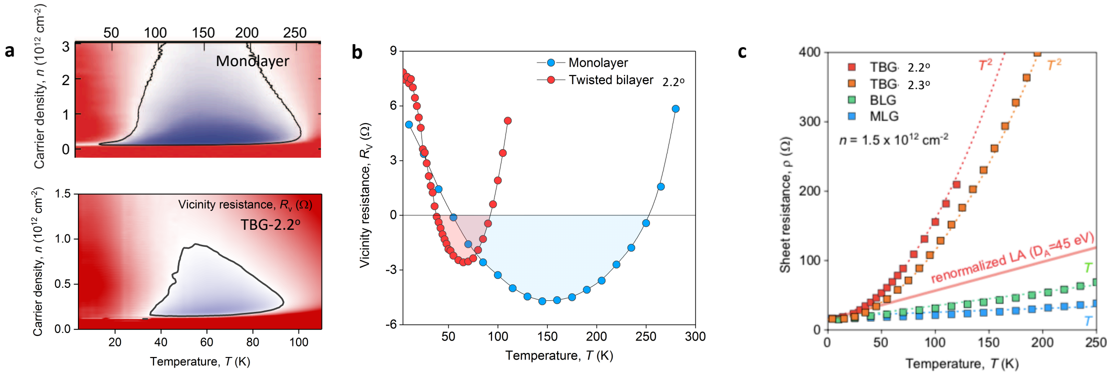

Figure 3-3: Vicinity resistance versus temperature in SA-TBG. **a)** Top: vicinity resistance for monolayer graphene. Bottom: vicinity resistance for TBG-2.2°. Note that the regime of negative vicinity resistance in TBG-2.2° is much smaller in area, extending to a smaller extent in both n and T. Monolayer data adapted from [1]. **b)** Line-cut at $n = 0.25(10^{12}\,\mathrm{cm}^{-}2)$ for monolayer (blue) and TBG-2.2° (red). **c)** Longitudinal resistivity versus temperature for monolayer (blue), bilayer (green), and SA-TBG (red and orange) devices. Note that the SA-TBG devices show a much stronger increase in resistivity.

Fermi velocity to determine twist angle. For both devices, we also determine the effective mass as a function of carrier density using the methods outlined previously.

We first characterized the two devices in the ballistic and diffusive regimes. As shown in Fig. 3-2b and e, both devices display a narrow Dirac peak, indicating low charge inhomogeneity. We then performed transverse magnetic focusing (TMF) and bend resistance measurements to determine the ballistic behavior. Both devices, as in Fig. 3-2c and f, showed clean TMF and negative bend resistance.

Having determined that at low temperatures, our devices were ballistic, we began to increase the temperature and to see if we could observe hydrodynamic behavior. Following previous experiments [1, 2, 4, 26] and theoretical work [51, 33, 37], we measured vicinity resistance as shown in Fig. 2-3e. As shown in Fig. 3-3a, we see negative vicinity resistance, a signature of the onset of fluidity. However, as shown in Fig. 3-3b, in comparison to graphene, although the crossover regime in TBG sets in at a lower temperature, it spans a much smaller range than in monolayer graphene.

As we measured ρ_{xx} with increasing temperature, we noticed something interesting: in graphene $\rho_{xx}(T)$ weakly increases with temperature, but in TBG, we see a rapid increase in resistivity up to kΩ at room temperature (Fig. 3-3c). Plotting the temperature dependence alongside a linecut of the vicinity resistance as in Fig. 3-3b and c, we see that this rapid increase in resistivity is what is damping the negative vicinity resistance. In other words, we witness a competition between momentum-conserving interactions (hydrodynamic) and momentum non-conserving interactions (mechanisms causing the rapid increase in ρ_{xx}) in overlapping regimes in the same device. The fact that negative vicinity resistance appears at all in SA-TBG devices is remarkable, particularly given the nearly 10-fold increase in resistivity at 100 K as compared to monolayer. The exact nature of the viscous regime in SA-TBG devices requires further exploration —in particular, it would be useful to measure the kinematic and Hall viscosities and compare these values to those previously obtained for monolayer graphene [1, 4]. Experimentally, the Hall viscosity will require the ability to apply magnetic field over the regime of negative vicinity resistance (up to 100 K), which is not possible in the Janis He-3 system we used.

3.4 Conclusion - competing interactions

We observe the onset of fluidity in SA-TBG devices via vicinity resistance transport measurements. Additionally, a competition between momentum-conserving and momentum non-conserving scattering processes appears in the same device. This behavior is markedly different from previous measurements in mono- and bilayer graphene. Our observations opens avenues for interesting studies of the crossover between these two regimes and raises the question: what are these momentum non-conserving interactions? We address this question in the following chapters.

Chapter 4

Enhanced resistivity in SA-TBG

Summary: For twist angles between 0 and 4°, we measure $\rho_{xx}(T)$ for temperatures from $4\,K$ to $300\,K$. We observe that $\rho_{xx}(T)$ increases much more strongly as a function of temperature than in mono- or bilayer graphene, and moreover shows a strong dependence on twist angle in both magnitude and also functional dependence. Previous work at smaller angles suggested a linear-in-temperature dependence due to phonon-scattering, citing an electron-phonon coupling mechanism similar to that in metals. We find evidence that this behavior does not persist at larger twist angles.

4.1 Introduction - temperature-dependent resistance in TBG

It is generally known to experimentalists working with SA-TBG that, near the magic angle, devices exhibit longitudinal resistivity with unusually strong temperature dependences, reaching several kΩ by 20 K [39, 10]. As shown in chapter 3, we see a strong increase in resistivity at larger angles as well. The mechanisms that cause this strong increase in resistivity —and whether they are the same across all twist angles or if they are an amalgamation of separate, competing mechanisms— is an interesting topic because they have to do with how momentum is relaxed in SA-TBG. In particular, they may be related to the superconductivity observed in SA-TBG devices around the magic angle.

4.2 Background

The functional dependence of resistivity on temperature is an important question for nearly all condensed matter systems. For example, efforts to understand momentum-relaxation mechanisms in metals have been going on since well into the 1900's. Although the simple picture we are taught in elementary electricity and magnetism claims that resistance is linear with temperature in a metal wire, reality proves very different. As just one example of many, aluminium at low temperatures has been shown to have a $\propto T^2$ component in resistivity. The mechanism behind this was subject to several theoretical papers in the 1970's and 1980's [31, 35, 36]. At the risk of giving away the rest of this chapter, we note that, surprisingly, these mechanisms may be related to the observed quartic temperature dependence we observe in SA-TBG at larger twist angles, although much experimental and theoretical work remains to be done.

Previous work on the temperature dependence of resistivity in SA-TBG found a linear-in-temperature dependence for angles near 1.1° [39, 8]. The mechanism that Ref. [39] found fit their experimental results relies on quasielastic scattering of electrons on acoustic phonons, somewhat similar to the mechanisms that describe the temperature dependence in superconducting metals [34, 39]. The model they present is the following:

$$\rho = \frac{\pi F D_A^2}{g e^2 \hbar \rho_m v_F^2 v_{ph}^2} k_B T \tag{4.1}$$

where D_A is the deformation potential describing the strength of electron-phonon coupling, $\hbar$ is the reduced planck's constant, e is the charge of an electron, k_B is Boltzmann's constant, v_F is the Fermi velocity, v_{ph} is the speed of sound, ρ_m is the mass density, g is the degeneracy in TBG (8), and F is a form factor that is approximately 0.5 for TBG. The model applies at low carrier densities, when the Fermi surface is smaller than the Brillouin zone (BZ). Because of the v_F^{-2} factor, the authors find that the renormalization of the Fermi velocity near the magic angle can account for the drastic increase in resistivity, assuming large enough electron-phonon coupling. This explanation, which offers a single mechanism to account for the behavior observed at a range of twist angles near 1.1°, is in disagreement with other theories [8], which posit that, rather than a metal-like relaxation mechanism, magic-angle graphene displays strange metal-like behavior with quantum fluctuations being the source of large linear-in-temperature resistivity.

With these differing explanations in mind, we now move on to exploring the temperature dependence of resistivity ourselves.

4.3 Results

We measure $\rho_{\mathrm{xx}}(T)$ in four devices with twist angles above the magic angle and one below. We use the same naming conventions as before for devices of twist angles 0.5°, 1.65°, 2.2°, 2.3°, and 4°. All devices are characterized as described in chapter 2 and exhibit ballistic transport over long distances at low temperatures (Figs. 3-2 and 4-1). The angles of TBG-2.2° and TBG-2.3° were determined by the suppression of Fermi velocity and Brown-Zak oscillations, respectively. In TBG-1.65°, we were able to reach full filling of the minibands to determine the angle. Two of the devices, namely TBG-0.5° and TBG-4°, have large uncertainties on the angle because we do not have enough data at the present time to determine the angle accurately. However, we have calculated bounds on the possible angles with the available data, and label them by an esimate of the angle. For comparison, we also consider hBN-encapsulated monolayer graphene (MLG) and bilayer graphene (BLG) devices. These devices were fabricated following the same processes and also exhibit ballistic transport at low temperatures.

Fig. 2-4a compares the low-temperature resistivity, $\rho(n, T)$, of large-angle TBG and MLG. The two are nearly identical and show the same narrow Dirac peak, demonstrating low charge inhomogeneity. In fact, at low temperatures away from the neutrality point, all five devices exhibit similar $\rho(n, T)$ values of 20-40 Ω. The low sheet

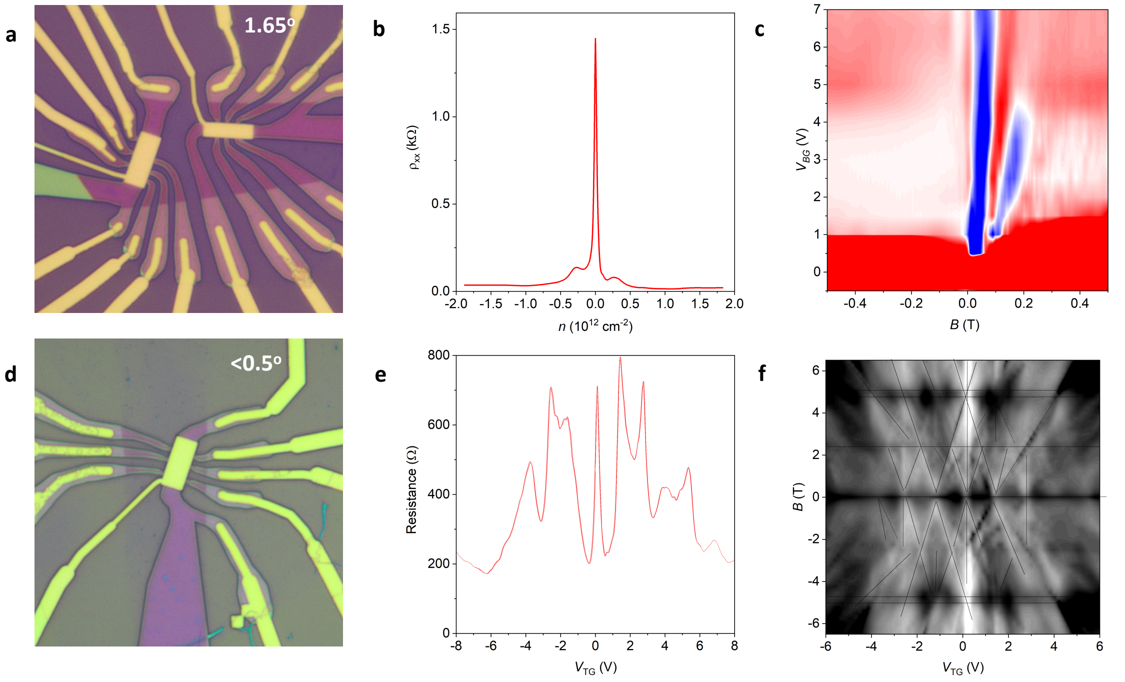

Figure 4-1: Device characterization for TBG-1.65° and TBG-0.5°. **a)** Optical image of TBG-1.65°. The Hall bar measured is the rightmost of the two shown. **b)** Narrow Dirac peak for TBG-1.65°. We do not currently know the origin of the small bumps on either side of the Dirac peak, but find they do not have a functional dependence on gating or magnetic field. **c)** TMF for TBG-1.65°. The apparent difference in quality between TMF for this smaller angle device in comparison to TBG-2.2° and TBG-2.3° is likely due to trigonal warping of the Fermi surface, which will be enhanced at smaller angles. The device also displays negative bend resistance, so we can be fairly confident that the device is ballistic at low temperature. **d)** Optical image of TBG-0.5°. We do not currently have enough data to determine the exact twist angle of the device. **e)** Narrow Dirac peak for TBG-0.5° as well as secondary peaks that are suppressed by increasing temperature. The large offset from zero may be due to a poor contact. **f)** Landau fan at 4 K displaying a Hofstadter butterfly. Black lines guide the eye. We do not yet have ballistic transport data for this device, but the cleanliness of the Landau fan indicates the device is of high quality.

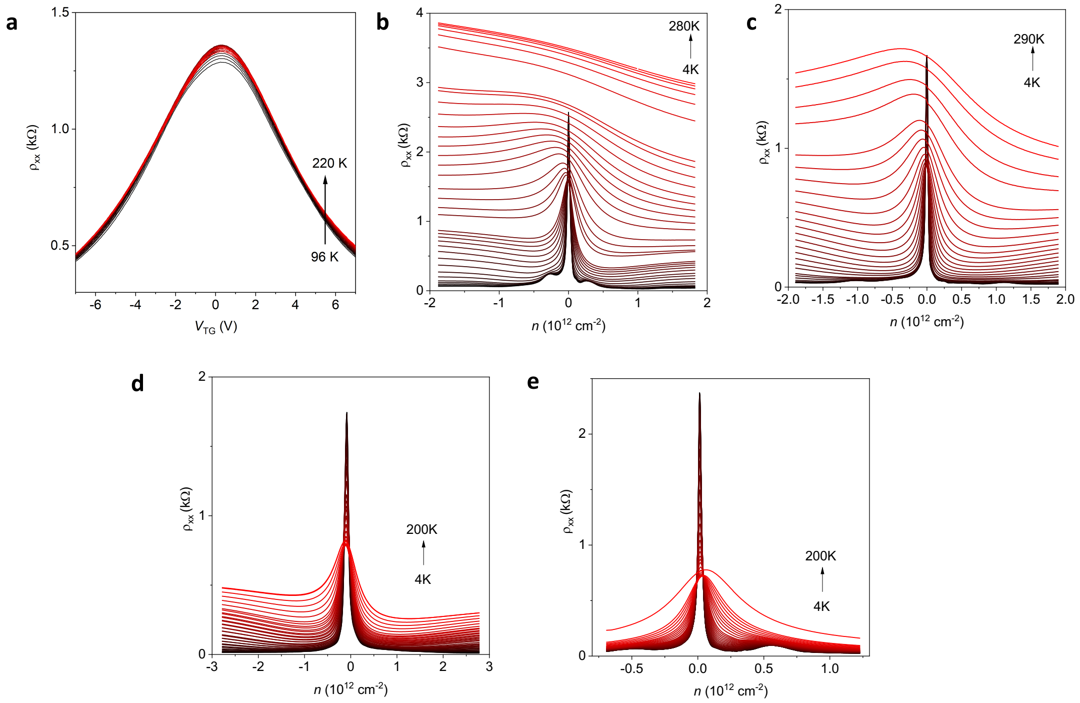

Figure 4-2: Resistivity versus carrier density for a range of temperatures in five devices. **a)** $\rho_{xx}(T)$ vs. n for $T = 96$ to $T = 220\,\text{K}$ in TBG-0.5°. Note that at low temperatures (Fig. 4-1), ρ_{xx} has several secondary peaks that are suppressed with temperature. **b)** $\rho_{xx}(T)$ vs. n for TBG-1.65° from 4 K to 280 K. Note this device reaches the highest values of resistivity and exaggerated thermal broadening. **c)** $\rho_{xx}(T)$ vs. n for TBG-2.2° from 4 K to 290 K. **d)** $\rho_{xx}(T)$ vs. n for TBG-2.3° from 4 K to 200 K. **e)** $\rho_{xx}(T)$ vs. n for TBG-4° from 4 K to 200 K.

resistance coupled with the narrow Dirac peaks in Figs. 3-3, 3-2, and 4-1 are an indicator of high-quality, clean 2DEGs. The high-temperature resistivity of the TBG devices differs widely from that of monolayer: as shown in Fig. 3-3c, MLG and BLG are linear in T. However, in Fig. 4-2, we see that, for all angles, the TBG resistivity is strongly enhanced and the Dirac peak is broadened, as expected, due to thermal excitations. The linear $\rho(T)$ dependence in MLG and BLG is in agreement with phonon-impeded transport [39, 34]. In contrast, we find that SA-TBG exhibits much faster growth in $\rho(T)$ over a range of n (Fig. 4-2 and 4-3). Note we restrict ourselves to small fillings where the Fermi surface is small in comparison to the first BZ. Therefore, this approximately $\propto T^2$ dependence appears in a regime where conventional Umklapp scattering —a known mechanism for T^2 behavior— cannot occur.

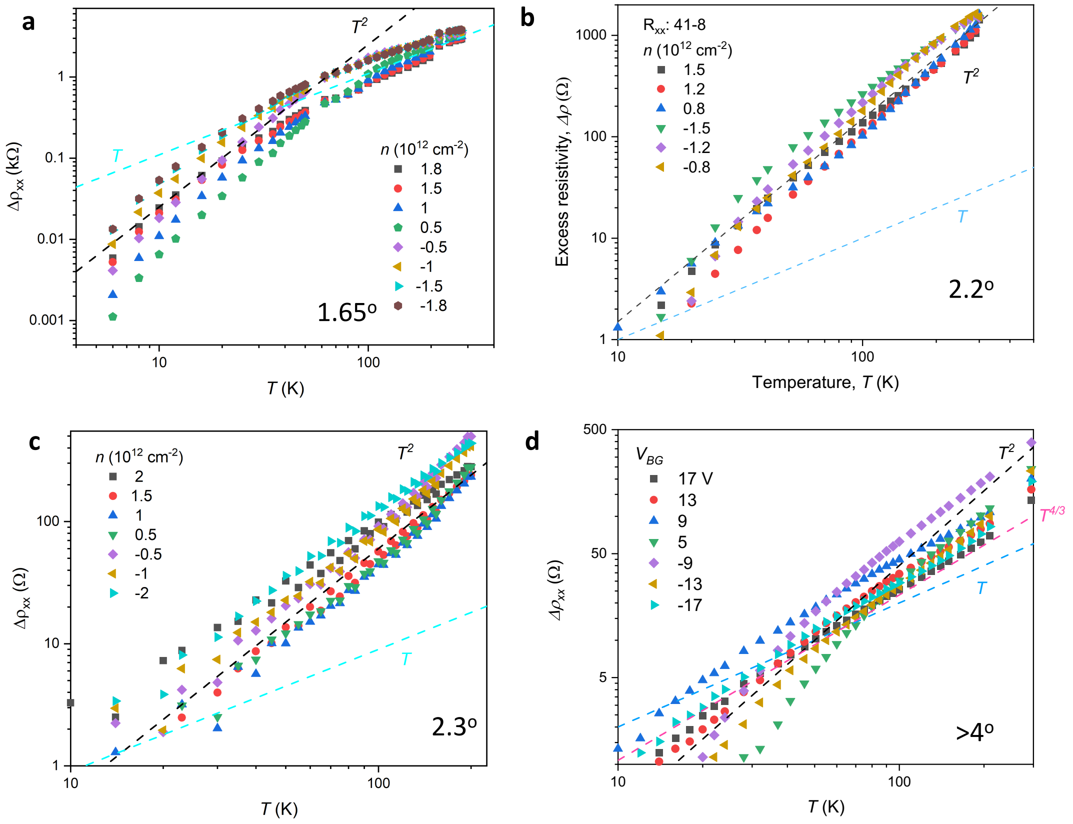

Figure 4-3: Log-log plots of excess resistivity versus temperature for devices above the magic angle at a range of carrier densities. **a)** $\Delta\rho_{xx}$ vs. T for TBG-1.65° at a characteristic range of carrier densities for both electrons and holes. At lower temperatures, $\Delta\rho_{xx}$ follows a T^2 dependence, but saturates to a linear-in-T dependence at higher temperature, in agreement with [39]. **b)** $\Delta\rho_{xx}$ vs. T for TBG-2.2°, displaying a clear T^2 dependence for a wide range of carrier densities. **c)** $\Delta\rho_{xx}$ vs. T for TBG-2.3°, again displaying a strong T^2 dependence for a wide range of carrier densities. **d)** $\Delta\rho_{xx}$ vs. T for TBG-4°, displaying a T^2 dependence for smaller carrier densities and a super-linear dependence ($\approx T^{4/3}$) for larger carrier densities.

We consider the excess resistivity, $\Delta\rho(T) = \rho(T) - \rho(4\text{K})$, which captures the temperature-dependent portion of $\rho(T)$ (Fig. 4-3). Focusing now on only twist angles above the magic angle, a log-log plot clearly demonstrates that $\Delta\rho(T)$ closely follows a T^2 dependence for a wide range of carrier densities for TBG-2.2° and TBG-2.3°. However, although TBG-1.65° initially follows a T^2 dependence at lower temperatures, the dependence becomes linear at higher temperatures. Ref. [39] found similar behavior, and our results are in agreement with devices of similar angle that they measured (i.e. Fig. 3 of [39]). For TBG-4°, the excess resistivity follows a T^2 dependence for small carrier densities, but decreases to a superlinear, approximately $T^{4/3}$, dependence for larger carrier densities. Additionally, it displays similar behavior to TBG-1.65° in that at low temperatures, the excess resistivity at all carrier densities displays stronger functional dependence on temperature than at higher temperatures.

We note an asymmetry in ρ_{xx} for electrons and holes in three of the devices, which results in some slight difference in the temperature dependence of ρ_{xx} for similar $|n|$. Calculations of the band structure show an asymmetry in electron and hole bands, which may play a role in the observed asymmetry, possibly through differences in carrier-phonon coupling. Previous works have also noted discrepancies between the electron and hole sides, and attribute this to asymmetric band structure [39].

Before moving on to the next section, we wish to give a quick look ahead to chapter 5, where we will find evidence for a mechanism that could potentially serve as an explanation for the observed T^2 behavior. In the next chapter, we will observe the presence of magnetophonon oscillations in TBG-1.65°, TBG-2.2°, and TBG-2.3°. At high carrier densities, we can see their contribution even below 10K, where they appear in conjunction with SdHO. From the acoustic phonon spectrum, we can estimate the energy and momentum of the active phonons and will hypothesize a possible mechanism for the observed resistivity. For now, however, we will consider other possible mechanisms.

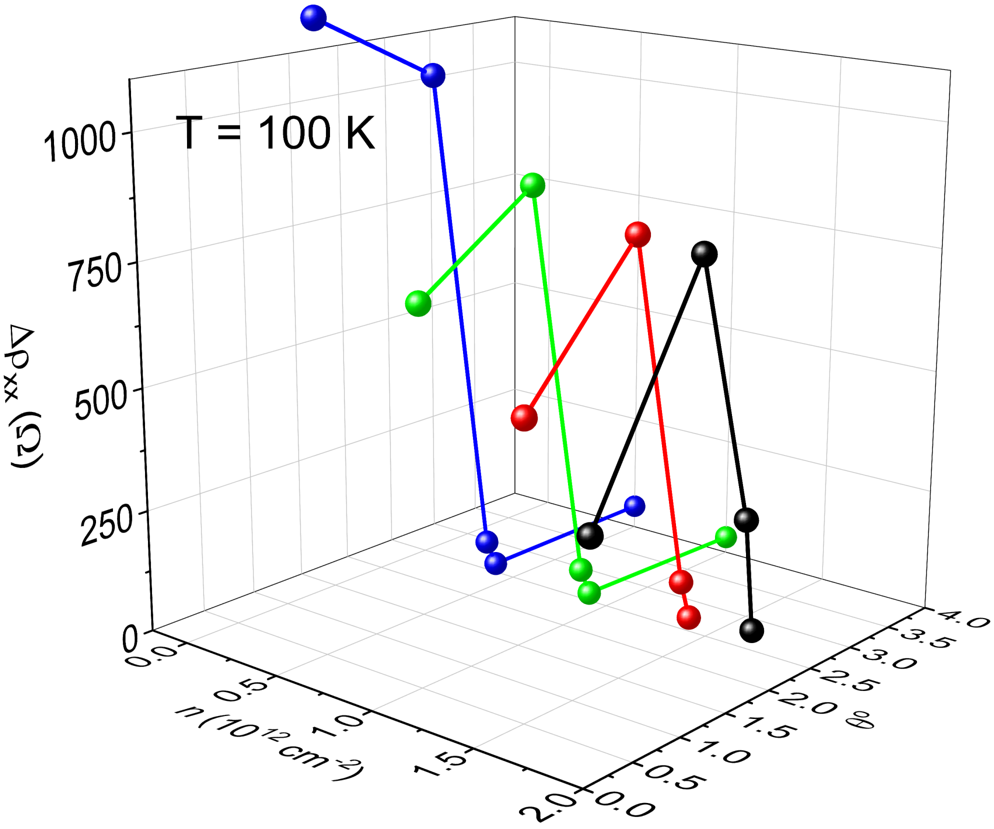

Figure 4-4: Summary of excess resistivity versus electron density and angle at $T = 100\,K$. $n = 1.8 \times 10^{12}\text{cm}^{-2}$ (black), $n = 1.5 \times 10^{12}\text{cm}^{-2}$ (red), $n = 1.0 \times 10^{12}\text{cm}^{-2}$ (green), $n = 0.5 \times 10^{12}\text{cm}^{-2}$ (blue). Note that the excess resistivity increases around the magic angle and decreases to either side, for larger and smaller angles.

4.4 Conclusion - explanations for T^2 behavior

We first wish to exclude the possibility of quasielastic electron-phonon scattering as given in Ref. [39]: we note the simple renormalization of the Fermi velocity in TBG cannot explain the T^2 behavior. In particular, considering Fig. 3-3c, the Fermi velocity of bilayer graphene (green) is close to that of TBG-2.2° (red), but they clearly exhibit greatly differing behavior. Assuming a deformation potential of 45 eV, and following theoretical work, we may plot the sheet resistance contribution by phonon-mediated relaxation, which we plot in the same figure as a red line [34, 39]. Even a generous estimation for the deformation potential, such a model cannot reach the rapid growth in $\rho(T)$ that we observe.

As previously shown in graphene-hBN superlattices [27], the superlattice potential can have an extreme effect on resistivity, causing, for example, the nearly constant-in-temperature resistivity of monolayer graphene to switch to a strong T^2 dependence when aligned with hBN, an insulator with a similar lattice constant. Such an effect is due to the creation of a mini-BZ around the Dirac points, with length scales determined by λ, the reciprocal superlattice vector. Since $\lambda \gg a$ for small angles (less than $\approx 15°$), the reciprocal superlattice vector is much smaller than the reciprocal lattice vector of graphene, and thus Umklapp scattering processes can occur despite the weak electron-phonon coupling of graphene.

Following this line of thought, we posit a simple picture that explains the observed quadratic dependence as well as the crossover to a linear regime for high carrier densities for holes. We consider a two-electron scattering process between the K and K' points of the mini-BZ. The two electrons can scatter from one side of the Fermi surface around the K point, for example, to the opposite side of the Fermi surface around the K' point, yielding a total change in momentum

$$\Delta k = 2k_F + \frac{G}{\sqrt{3}} - (-2k_F). \tag{4.2}$$

If $\Delta k = G$, such processes are allowed. This yields $k_F = \frac{12G}{3\sqrt{3}-\sqrt{3}} \approx 0.1G$. For TBG-2.2°, we achieve such a condition at $n \approx 0.6 \times 10^{12}$ cm^{-2}.

We note such a two-electron process may account for the T^2 dependence. As carrier density is increased, however, we observe a linear trend for TBG-1.65° and TBG-4°. If we consider the same picture but instead for single electron-phonon scattering processes, Δk changes to

$$\Delta k = k_F + \frac{G}{\sqrt{3}} - (-k_F) \tag{4.3}$$

and thus our requirement on the Fermi momentum is now $k_F \approx 0.2G$. This equates to a carrier density of $n \approx 2.4 \times 10^{12}\ \mathrm{cm}^{-2}$, in agreement with experimental observation. However, the rate at which these electron-electron and electron-phonon scattering processes occur may not be high enough to justify the T^2 behavior, so this scenario requires additional thought.

Alternatively, we can explain the T^2 behavior as a result of moiré phonons in twisted bilayer. As described in chapter 5, magnetophonons are present in all three larger-angle devices and correspond well to transverse shear phonon branches. Because the moiré pattern results in mini-BZ that are much smaller than the graphene BZ, we can achieve inter-layer scattering from phonons between the valleys of the mini-BZ. We elaborate on this scenario in the next chapter.

Chapter 5

Observation of Magnetophonon Oscillations in TBG

Summary: We observe magnetophonon oscillations in TBG devices above the magic angle. By studying the carrier density dependence, we are able to identify potential shear phonon modes. Our observations allow us to develop a potential explanation for the T^2 resistivity observed previously, and also have implications for further studies on phonon-driven phenomena in SA-TBG.

5.1 Introduction - magnetophonons in graphene

As mentioned previously, we noticed that the SdHO, while strong and cleanly periodic in the TBG devices, seem to have a strange beating pattern that modifies the normal $\lambda \sinh(\lambda)$ envelope (visible in Fig. 2-7a). Increasing the sample temperature causes the SdHO to be rapidly damped, decaying to 0 by 15 K or so. At around this temperature, a new pattern emerges with a longer period than the SdHO and an entirely different temperature dependence. It is this new, higher-temperature oscillation that we will study in this chapter.

5.2 Background

5.2.1 A brief introduction to phonons

Phonons are quantized vibrations of the crystal lattice. We can group them into acoustic and optical modes: acoustic modes refer to coherent (in-phase) movement of atoms, while optical modes are out-of-phase movement in crystals with a 2+ atom basis (such as graphene). Typically, the optical modes are much higher energy than the acoustic modes. We can further break down the modes into branches with reference to their direction of propagation and direction of oscillations: transverse (oscillation $\perp$ propagation) and longitudinal (oscillation $\parallel$ propagation). For a 2D system, we can also have both in-plane and out-of-plane motion. And finally, for a bilayer system, we can also have layer-symmetric and layer-antisymmetric modes. In our work, we will consider only acoustic branches and use following naming conventions:

In-plane transverse acoustic	TA
In-plane longitudinal acoustic	LA
Out-of-plane acoustic	ZA
Layer-symmetric	subscript$_1$
Layer-antisymmetric	subscript$_2$

5.2.2 Magnetophonon resonances in monolayer graphene

Previously, magnetophonon oscillations were observed in extra-large monolayer graphene devices [29]. In monolayer graphene, the devices must be wider than 10 μm in order for multiple orbits fit within a single device and for resonant scattering to occur. Recall that in an applied magnetic field, B, charge carriers become localized in closed orbits, and the electronic spectrum of charge carriers in graphene form quantized Landau levels (LL) which are unequally spaced in energy. An electrical current can still flow, however, because charge carriers can scatter from nearby orbits with assistance from phonons to satisfy energy and momentum conservation, or move in skipping orbits along the edge of the system. As shown in Fig. 5-1b, in a semi-classical picture, the first scenario can be thought of as electrons jumping between two orbits that touch

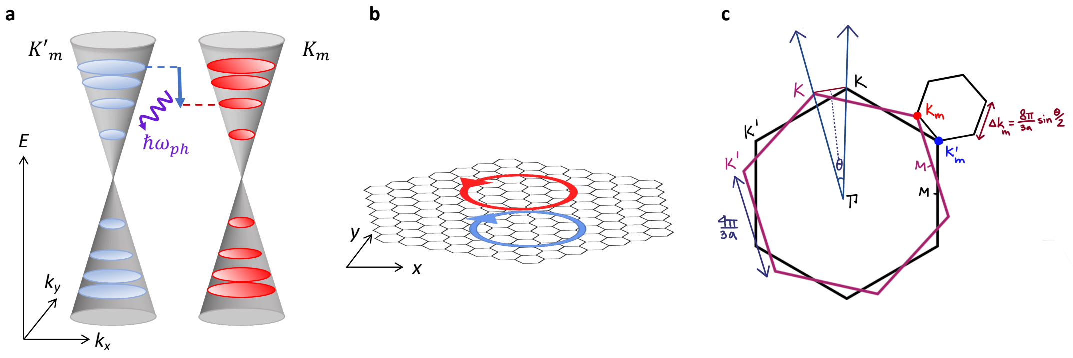

Figure 5-1: Mechanisms for magnetophonon resonances in MLG and TBG. **a)** An electron scatters from a higher energy Landau level (LL) to a lower energy level by emission of a phonon with energy equal to the difference in energies of the LL. **b)** The same process but illustrated in real-space. An electron moving in a left-circularized cyclotron orbit jumps to a neighboring, right-circularized orbit by emission of a phonon with momentum equal to the electron's change in momentum. **c)** The mini Brillouin zone of SA-TBG with various quantities in k-space labelled. The distance between K_m and K'_m points of the mini BZ is $\frac{8\pi}{3a}\sin(\theta/2)$, a quantity that will be important to us later.

in real space, or, in quantum terms, where the wavefunctions just barely overlap at the touching points. In reciprocal space, as shown in Fig. 5-1a, an electron jumps between LL with the emission or absorption of a phonon of energy equal to the difference in LL spacing. Because the phonons involved in this process must have energy equal to LL spacings, this forms a resonant condition, which we call magnetophonon resonance, that is observed as resistance oscillations periodic in B^{-1}.

The resonance condition is as follows: for a carrier scattering between cyclotron orbits as in Fig. 5-1b, the phonon must have momentum $q \approx 2k_F$ since the velocity of the electron is reversed. Assuming a roughly linear acoustic phonon dispersion, $\hbar\omega = \hbar v_s q$, where v_s is the speed of sound, and recalling the LL energy spectrum, we see that the energy of the phonon $\hbar\omega_{\text{ph}}$ must be equal to the difference in LL energy,

$$\hbar\omega_{\text{ph}} = \hbar\frac{v_s}{l_B}(\sqrt{2(N \pm p)} + \sqrt{2N}) = \pm\frac{\hbar v_F}{l_B}(\sqrt{2(N \pm p)} - \sqrt{2N}) \tag{5.1}$$

where $\omega_c = \frac{v_s}{l_B}$, l_B the quantum magnetic length, $\sqrt{\hbar/eB}$, and N and p label the starting $(N \pm p)^{\text{th}}$ LL and the final $(N)^{\text{th}}$ LL.

Expanding and taking the limit $v_F >> v_s$, we get

$$N \approx \frac{p v_F}{4 v_s} \tag{5.2}$$

Then, noting that the LL index near the Fermi energy can be approximated as $N = hn/4eB$, where n is the carrier density, we find the full resonance condition:

$$B_p \approx \frac{n h v_s}{p e v_F} \tag{5.3}$$

Off resonance, the current will only be due to skipping orbits along the edge of the sample. On resonance, an additional dissipative current will appear as scattering between neighboring cyclotron orbits is allowed. The conductivity will have the form

$$\Delta\rho_{xx} \propto e^{-\gamma/B} \cos(2\pi p B_p/B) \tag{5.4}$$

where γ is a damping term related to temperature. We emphasize two features: the resistivity has a $1/B$ periodicity, and the fundamental frequency pB_p is linear in n.

Turning to magnetophonons in TBG, noting $k_F = \sqrt{\pi n/2}$ for an 8-fold degenerate Fermi surface, we get the simplified resonance condition

$$B_F \equiv p B_p = \frac{\omega_{\mathrm{ph}} m_c}{e} \tag{5.5}$$

taking the phonon frequency $\omega_{\mathrm{ph}} = v_s q = 2 v_s k_F$ and the cyclotron mass $m_c = \hbar k_F / v_F$.

5.3 Results

We measured three devices composed of SA-TBG encapuslated in hBN crystals, fabricated using the tear-and-stack and hot-release methods described previously. We label the devices by their angle as before: TBG-1.65°, TBG-2.2°, and TBG-2.3°. As shown in Fig. 3-2 and 4-1, we characterized the devices and demonstrate low charge disorder and ballistic transport at 4 K. The angles were determined as previously

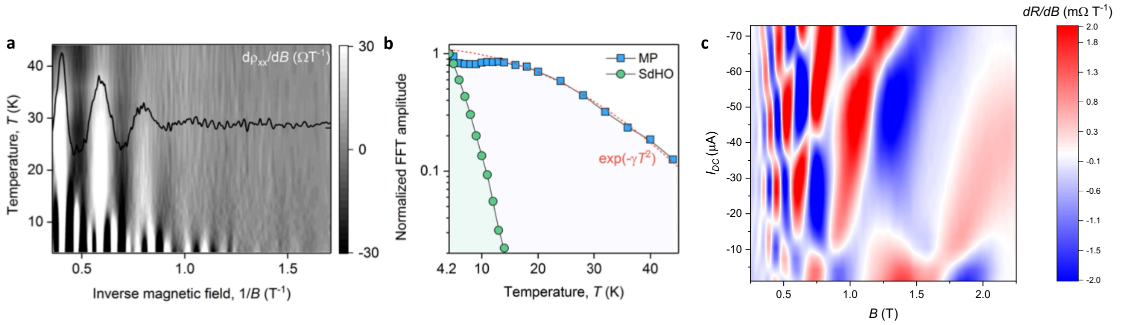

Figure 5-2: Magnetophonons versus Shubnikov de haas oscillations. **a)** $\partial\rho_{xx}/\partial B$ vs. $1/B$ as a function of temperature for $n = 2.77 \times 10^{12}\,\mathrm{cm}^{-2}$ for TBG-2.3°. SdHO are clear at low temperatures, appearing as sharp black and white vertical lines at the bottom of the map. As temperature is increased, lower frequency magnetophonon oscillations (MPO) appear. A linecut of $\partial\rho_{xx}/\partial B$ vs. $1/B$ at $T = 20\,K$ is shown in black. **b)** The normalized magnitudes of SdHO and MPO, obtained by FFT analysis, are plotted as a function of temperature. MPO occur over a much broader range of temperatures, but notably occur at low temperatures as well, at the same time as SdHO are present. **c)** $\partial\rho_{xx}/\partial B$ versus B as a function of I_{DC} at 20 K. The phase of MPO have been shown to be sensitive to an applied DC bias [59]. We see evidence of the phase shift as a function of the applied bias I_{DC} in the checkerboard pattern visible here.

described in section 4.3.

At 4 K, all three devices show SdHO with fundamental frequency $B_F = nh/8e$ as expected. The SdHO are suppressed with increasing temperature, vanishing by 15 K or so. As mentioned, a new set of magneto-oscillations appears above 15 K with a larger period and sustains up to 50 K. These oscillations are identified as magnetophonon oscillations (MPO). They are most apparent in TBG-2.3°, which also has the most accurate angle determination, so we focus primarily on this device in the following analysis.

We first wish to definitively separate SdHO and the observed MPO and prove that they are two entirely different oscillations. We note that the temperature dependence of MPO and SdHO are very different (Fig. 5-2a). The MPO extend beyond 45 K and persist down to liquid helium temperatures, appearing at low temperatures as a modulation on top of the higher frequency SdHO, as shown in Fig. 5-2b. Next, we notice that, in the presence of a DC bias, the phase of the MPO can be switched as a function of the applied bias, as shown in Fig. 5-2c. The general dependence of MPO phase on DC bias has been observed previously in other systems [59, 15]. SdHO, on the other hand, are immediately killed by the application of a DC bias when we perform the same measurements at liquid-helium temperatures and only MPO oscillations remain, again showing the same "checkerboard pattern" of phase shift.

Having conclusively determined that the MPO and SdHO are two very different types of oscillations, we investigate the behavior of the MPO more closely. Plotted as a function of $1/B$ (Fig. 5-3b), we see the same $1/B$ periodicity as predicted in Eq. 5.4. In order to find the fundamental frequency, we plot the peaks $1/B_N$ as a function of extrema number N, where the inverse slope gives us B_F (Fig. 5-3c). Moreover, a Fast Fourier Transform (FFT) investigation of the phonon spectra shows us it is dominated by a single frequency (Fig. 5-3d), and thus, we can conclude a single phonon mode. We use this FFT spectra for TBG-1.65° in order to separate the SdHO and MPO because both coexist in the sample at similar temperatures.

We then consider the MPO dependence on carrier density. As shown in Fig. 5-3b-d, as expected from Eq. 5.3, we see that the B_F of MPO depends on the carrier density n. The dependence diverges from linear-in-n due to the non-linear dependence on n of the renormalized v_F. From the FFT, we also note that the magnitude of the oscillations decrease with $|n|$. In Fig. 5-3e, we compare $B_F(n)$ as a function of carrier density against $B_F(n)$ for monolayer graphene, and note the significant difference between the functional behavior between the two [29].

In order to compare the phonons measured in our TBG devices to theoretical calculations [25, 11], we calculate the phonon energy

$$\hbar\omega_{\text{ph}} = \hbar e B_F(n)/m_c(n) \tag{5.6}$$

applying Eq. 5.5 and taking $m_c(n)$ from our measurements of effective mass. The result is plotted in Fig. 5-4a.

Now we wish to compare these phonon energies with the previously derived intra-

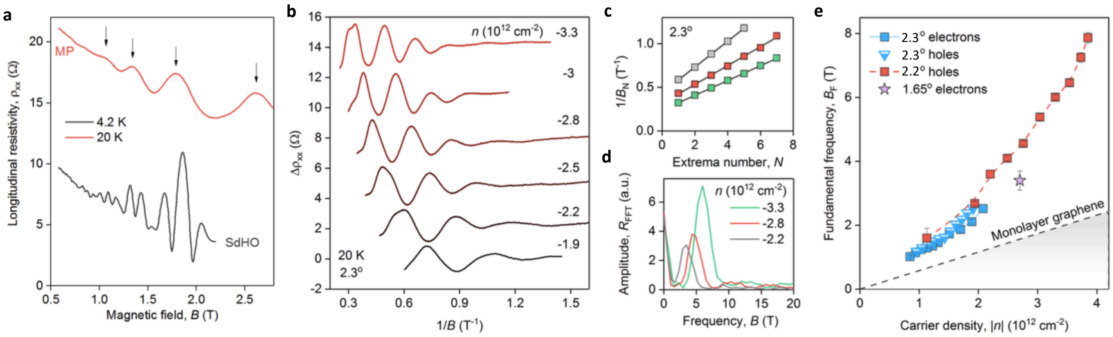

Figure 5-3: Behavior of Magnetophonon resonances as a function of carrier density and inverse magnetic field for TBG-2.3° unless otherwise noted. **a)** SdHO at liquid-helium temperatures and MPO at 20 K vs. B. The difference in period is very apparent when plotted together. Black arrows indicate the peaks of MPO used to determine the fundamental frequency. **b)** MPO vs. $1/B$ plotted for comparatively high carrier densities, labelled on the right side of the graph. The resonant condition and the amplitude both show dependence on n. **c)** Peaks of MPO vs. peak number gives us the fundamental frequency B_F. $n = -2.2 \times 10^{12}\text{cm}^-2$ (grey), $n = -2.8 \times 10^{12}\text{cm}^-2$ (red), $n = -3.3 \times 10^{12}\text{cm}^-2$ (green). **d)** FFT spectra of MPO, showing a decrease in amplitude as $|n|$ decreases. **e)** B_F vs $|n|$ for all three devices. B_F vs $|n|$ of monolayer graphene, obtained from [29], plotted in grey. The difference in functional behavior is apparent.

valley scattering mechanism observed in monolayer graphene. Recall this intra-valley scattering requires phonons of momentum $q = 2k_F$. Assuming a Dirac dispersion ($\hbar\omega_{ph} = qv_s$) and taking $v_s = 14\,\mathrm{m/s}$ as in MLG (figure 4 of [29]), we plot the expected $\hbar\omega_{\mathrm{ph}}$ in Fig. 5-4 (grey dashed line). We see that the expected values are several standard deviations below the experimentally determined values. This implies that the intra-valley scattering assumption $q = 2k_F$ from Eq. 5.6 and Eq. 5.3 is not applicable. Instead, if we consider phonons with $q > 2k_F$ and a different scattering mechanism, we can achieve a phonon energy matching our values. Such a situation is impossible in monolayer graphene: recalling that the radius of the Fermi surface is k_F, we note that the BZ is too large: the phonon momenta $\hbar q$ are not sufficient to allow phonon-assisted scattering between Fermi surfaces. But in TBG, the mini-BZ induced by the superlattice are much smaller (Fig. 5-1c). The six mini-valleys are then much closer in momentum space, allowing for scattering between the Fermi surfaces centered on these valleys. That is, the K_m and K'_m points of the mini-BZ (as labelled in Fig. 5-1) are separated by

$$\Delta K_m = \frac{8\pi}{3a}\sin(\theta/2) \tag{5.7}$$

meaning that we require phonons with energy only ΔK_m. The momentum of the measured phonons, assuming a roughly linear dispersion, will be

$$\hbar q = \hbar\omega_{\mathrm{ph}}/v_s \tag{5.8}$$

For example, estimating $v_s = 14\,\mathrm{km/s}$ from monolayer graphene [29], for TBG-2.2°, $\hbar\Delta K_m \approx 7 \times 10^{-26}\,\mathrm{Ns}$ and $\hbar q \approx 9 \times 10^{-26}\,\mathrm{Ns}$.

5.4 Conclusion - inter-valley scattering

Because the phonon dispersion has not been previously measured in TBG as far as we are aware, we turn to two theoretical papers for support [25, 11]. The main results are summarized in Fig. 5-4b and c. We primarily consider the low-energy dispersion

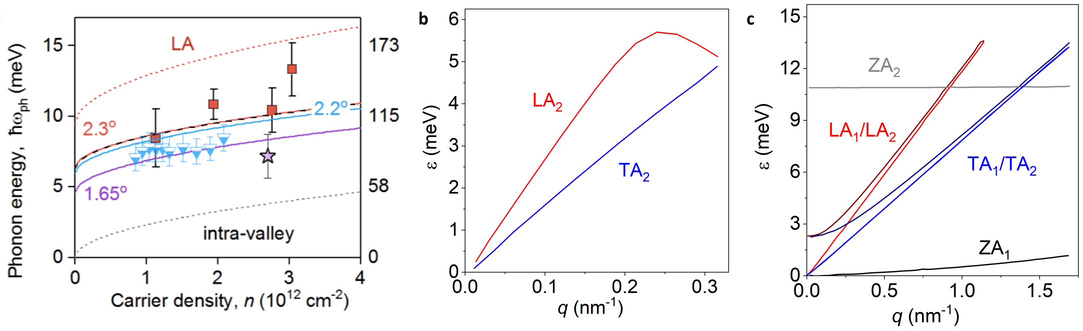

Figure 5-4: Phonon dispersions, both experimental and theoretically predicted. **a)** Phonon energy $\hbar\omega_{ph}$ vs. n, as measured. **b)** Low-energy phonon dispersion for layer-antisymmetric modes of 2.2° TBG from Ref. [25]. The linecut for q is taken between the Γ and K_m points. **c)** Phonon dispersion for bilayer graphene in the extended zone scheme along ΓK_m from Ref. [11]. Note the energy and momentum scales are different than in **b)**.

of the acoustic modes near the center of the first mini-BZ. Ref. [25] calculates only the in-plane layer anti-symmetric dispersion relations. We show the lowest two branches between the center and K_m point of the mini BZ (Fig. 5-4b). Ref. [11] calculates the acoustic phonon dispersion relations for bilayer graphene, not twisted bilayer (shown in the extended zone scheme in Fig. 5-4c). However, if we consider just layer-symmetric modes, we can make the rough estimation that small-angle TBG will have a similar dispersion relation to bilayer graphene, assuming that lattice vibrations will be dominated by the mechanical motions rather than coupling to the modified band structure, therefore we are justified in considering this dispersion as well.

We now want to figure out which phonon branch we observe. Comparing to the low-energy dispersion in Fig. 5-4c, we see that our phonon energies agree within error bars with the TA$_1$ and TA$_2$ branches for given wavevector q as in Eq. 5.8. For example, for TBG-2.2°, $\Delta K_m \approx 0.6\ \text{nm}^{-1}$, which corresponds to 4.7 meV in the TA$_2$ branch or 7 meV on the LA$_2$ branch. Ref. [25] gives 9 meV and 10 meV for the two branches respectively. We experimentally measure the value to be approximately 7 meV with error bars. We claim the ZA$_1$ and ZA$_2$ branches can be disqualified from consideration because the energy values are beyond error bars of our measured values. Additionally, previous studies have found that the LA branches do not couple strongly to electron transport [20, 57, 46, 15, 16, 48]. This leaves us with the TA branch as the most likely candidate.

We now consider inter-valley scattering within the mini BZ. As in Fig. 5-1c, the condition for phonon momentum for inter-valley scattering is $q = \Delta K_m + 2k_F$. Taking the dispersion relation previously, we can calculate the phonon energy $\hbar\omega_{ph}$ for the TA_1 and LA_1 branches, taking v_s for the respective modes from MLG. Because of higher group velocity of the LA mode, the LA_1 branch has higher energies than those measured (red dashed line in Fig. 5-4a). However, the energies calculated for the TA_1 branch match very well with those measured, shown as solid lines in Fig. 5-4 with no fitting parameters. The layer-symmetric and layer anti-symmetric branches have very similar energies (with differences smaller than the error bars on our measurements) at the q we consider, but for the sake of clarity, we note that the dispersion relation for the layer anti-symmetric branches should be $\omega = \sqrt{\omega_0^2 + v_s^2 q^2}$ [38]. Based on experimental evidence alone, we are unable to differentiate the layer symmetric and layer anti-symmetric modes. However, as in chapter 4, we observe a strong increase with temperature of resistivity, in agreement with other studies [39, 8]. As shown in Fig. 3-3c and explained in section 4.4, the resistivity contribution from the layer-symmetric TA mode does not match that observed. The layer anti-symmetric modes, however, may be able to capture the observed behavior.

The observations described in this chapter are relevant to understanding the mechanisms behind the strong increase in resistivity found in SA-TBG devices. We demonstrate that magnetophonon resonances provide a way to probe the superlattice-induced interactions in SA-TBG, in a way that has the potential to be applied more broadly, including near the magic angle. In particular, we untangle the phonon spectra of SA-TBG and find that layer anti-symmetric TA modes are likely the primary source of momentum-relaxation. As explained in chapter 4, understanding these momentum-relaxing mechanisms may be important to figuring out the nature of superconductivity in magic angle TBG.

Chapter 6

Conclusion and Future Directions

In this thesis, we explored superlattice-induced interactions in SA-TBG. We first considered the graphene viscous electron fluid and found evidence for the onset of fluidity in SA-TBG via negative vicinity resistance measurements. Strong interactions in SA-TBG have been proposed to provide a way to probe deeper in the hydrodynamic regime. However, we found the existence of a competing, momentum-non-conserving mechanism in the same carrier density and temperature phase space as the observed onset of fluidity. Exploring this mechanism further, we found that resistivity in SA-TBG at angles above ≈ 1.7 displays a T^2 dependence, a behavior that cannot be explained by previous linear-in-T theories. To explain this observation, we measured magnetophonon resonances in SA-TBG and found a potential T^2 mechanism that relies on inter-valley scattering within the mini-BZ. We also reconstructed the low-energy spectra for acoustic phonons and reasoned that layer anti-symmetric TA phonons are likely the primary source of momentum-relaxation. All these observations are tied together by a common thread: they show the effect of a superlattice on electron transport. When we measure the same quantities in mono- or bilayer graphene, we observe entirely different behavior. Through this we see the broad potential of moiré systems to realize many interesting phenomena.

One of the lingering questions from chapter 3 is whether or not there is a regime of twist angle in which the momentum-conserving interactions can “beat out” the momentum-non-conserving interactions so that we can see a strong negative vicinity resistance over a large phase space. One way to answer this would be to simply make more devices at both smaller and larger angles, and measure them. We can also study the nature of the viscous regime in TBG further: we have yet to measure the kinematic and Hall viscosity, which would be valuable to have to compare to the values found in MLG and BLG. However, we can also try to understand the nature of these momentum-non-conserving interactions as a function of twist angle to make predictions about whether such a regime exists. We attempt to do so in chapter 4 and chapter 5, but this question requires further study.

As mentioned in chapter 4, we still do not fully understand the origins of the giant increase in resistivity observed in SA-TBG devices, particularly near the magic angle. We provide one possible explanation in chapter 5, but this question needs to be more carefully explored. Perhaps most importantly, we want to know whether these electron-phonon interactions with shear phonons have anything to do with the mechanisms causing superconductivity. Generally, we want to know more about how electrons and phonons couple in SA-TBG devices.

Looking more broadly, recent proposals have suggested that the TBG could be used to realize non-Abelian states for topological quantum computing. For example, a recent proposal suggested TBG could be a host to a quantum spin Hall liquid [60]. Other proposals have suggested SA-TBG proximitized to a superconductor could be a host to Majorana bound states because fractional quantum Hall and quantum spin Hall states have been observed in the system [44, 55]. Following the observation of the quantum anomalous Hall effect in TBG, fractional Chern insulator states are also predicted to exist in TBG [45, 32]. In fact, in TBG-0.5°, we see evidence of fractional Chern insulators and are excited to pursue further study of this device. The list of fascinating phenomena in moiré systems is a long one, and in the future, both finding ways to access these phenomena and understand the mechanisms behind them will be important to condensed matter physics.

Bibliography

[1] D. A. Bandurin, I. Torre, R. Krishna Kumar, M. Ben Shalom, A. Tomadin, A. Principi, G. H. Auton, E. Khestanova, K. S. Novoselov, I. V. Grigorieva, L. A. Ponomarenko, A. K. Geim, and M. Polini. Negative local resistance caused by viscous electron backflow in graphene. *Science*, 351(6277):1055–1058, March 2016.

[2] Denis A. Bandurin, Andrey V. Shytov, Leonid S. Levitov, Roshan Krishna Kumar, Alexey I. Berdyugin, Moshe Ben Shalom, Irina V. Grigorieva, Andre K. Geim, and Gregory Falkovich. Fluidity onset in graphene. *Nature Communications*, 9:4533, October 2018.

[3] A. I. Berdyugin, B. Tsim, P. Kumaravadivel, S. G. Xu, A. Ceferino, A. Knothe, R. Krishna Kumar, T. Taniguchi, K. Watanabe, A. K. Geim, I. V. Grigorieva, and V. I. Fal'ko. Minibands in twisted bilayer graphene probed by magnetic focusing. *arXiv e-prints*, page arXiv:1911.02827, November 2019.

[4] A. I. Berdyugin, S. G. Xu, F. M. D. Pellegrino, R. Krishna Kumar, A. Principi, I. Torre, M. Ben Shalom, T. Taniguchi, K. Watanabe, I. V. Grigorieva, M. Polini, A. K. Geim, and D. A. Band urin. Measuring Hall viscosity of graphene's electron fluid. *Science*, 364(6436):162–165, April 2019.

[5] Rafi Bistritzer and Allan H. MacDonald. Moiré bands in twisted double-layer graphene. *Proceedings of the National Academy of Science*, 108(30):12233–12237, July 2011.

[6] Dan S. Borgnia, Trung V. Phan, and Leonid S. Levitov. Quasi-Relativistic Doppler Effect and Non-Reciprocal Plasmons in Graphene. *arXiv e-prints*, page arXiv:1512.09044, December 2015.

[7] Y. Cao, J. Y. Luo, V. Fatemi, S. Fang, J. D. Sanchez-Yamagishi, K. Watanabe, T. Taniguchi, E. Kaxiras, and P. Jarillo-Herrero. Superlattice-Induced Insulating States and Valley-Protected Orbits in Twisted Bilayer Graphene. *PRL*, 117(11):116804, September 2016.

[8] Yuan Cao, Debanjan Chowdhury, Daniel Rodan-Legrain, Oriol Rubies-Bigorda, Kenji Watanabe, Takashi Taniguchi, T. Senthil, and Pablo Jarillo-Herrero. Strange Metal in Magic-Angle Graphene with near Planckian Dissipation. *PRL*, 124(7):076801, February 2020.

[9] Yuan Cao, Valla Fatemi, Ahmet Demir, Shiang Fang, Spencer L. Tomarken, Jason Y. Luo, Javier D. Sanchez-Yamagishi, Kenji Watanabe, Takashi Taniguchi, Efthimios Kaxiras, Ray C. Ashoori, and Pablo Jarillo-Herrero. Correlated insulator behaviour at half-filling in magic-angle graphene superlattices. *Nature*, 556(7699):80–84, April 2018.

[10] Yuan Cao, Valla Fatemi, Shiang Fang, Kenji Watanabe, Takashi Taniguchi, Efthimios Kaxiras, and Pablo Jarillo-Herrero. Unconventional superconductivity in magic-angle graphene superlattices. *Nature*, 556(7699):43–50, April 2018.

[11] Alexandr I. Cocemasov, Denis L. Nika, and Alexand er A. Balandin. Phonons in twisted bilayer graphene. *PRB*, 88(3):035428, July 2013.

[12] M. J. M. de Jong and L. W. Molenkamp. Hydrodynamic electron flow in high-mobility wires. *PRB*, 51(19):13389–13402, May 1995.

[13] C. R. Dean, L. Wang, P. Maher, C. Forsythe, F. Ghahari, Y. Gao, J. Katoch, M. Ishigami, P. Moon, M. Koshino, T. Taniguchi, K. Watanabe, K. L. Shepard, J. Hone, and P. Kim. Hofstadter's butterfly and the fractal quantum Hall effect in moiré superlattices. *Nature*, 497(7451):598–602, May 2013.

[14] C. R. Dean, A. F. Young, I. Meric, C. Lee, L. Wang, S. Sorgenfrei, K. Watanabe, T. Taniguchi, P. Kim, K. L. Shepard, and J. Hone. Boron nitride substrates for high-quality graphene electronics. *Nature Nanotechnology*, 5(10):722–726, October 2010.

[15] I. A. Dmitriev, R. Gellmann, and M. G. Vavilov. Phonon-induced resistance oscillations of two-dimensional electron systems drifting with supersonic velocities. *PRB*, 82(20):201311, November 2010.

[16] I. A. Dmitriev, A. D. Mirlin, D. G. Polyakov, and M. A. Zudov. Nonequilibrium phenomena in high Landau levels. *Reviews of Modern Physics*, 84(4):1709–1763, October 2012.

[17] A. K. Geim and I. V. Grigorieva. Van der Waals heterostructures. *arXiv e-prints*, page arXiv:1307.6718, July 2013.

[18] A. K. Geim and K. S. Novoselov. The rise of graphene. *Nature Materials*, 6(3):183–191, March 2007.

[19] Steven M. Girvin and Kun Yang. *Modern Condensed Matter Physics*. Cambridge University Press, 2019.

[20] M. T. Greenaway, R. Krishna Kumar, P. Kumaravadivel, A. K. Geim, and L. Eaves. Magnetophonon spectroscopy of Dirac fermion scattering by transverse and longitudinal acoustic phonons in graphene. *PRB*, 100(15):155120, October 2019.

[21] R N Gurzhi. HYDRODYNAMIC EFFECTS IN SOLIDS AT LOW TEMPERATURE. *Soviet Physics Uspekhi*, 11(2):255–270, feb 1968.

[22] B. Hunt, J. D. Sanchez-Yamagishi, A. F. Young, M. Yankowitz, B. J. LeRoy, K. Watanabe, T. Taniguchi, P. Moon, M. Koshino, P. Jarillo-Herrero, and R. C. Ashoori. Massive Dirac Fermions and Hofstadter Butterfly in a van der Waals Heterostructure. *Science*, 340(6139):1427–1430, June 2013.

[23] A. Jenkins, S. Baumann, H. Zhou, S. A. Meynell, D. Yang, K. Watanabe, T. Taniguchi, A. Lucas, A. F. Young, and A. C. Bleszynski Jayich. Imaging the breakdown of ohmic transport in graphene. *arXiv e-prints*, page arXiv:2002.05065, February 2020.

[24] Charles Kittel. *Introduction to solid state physics.* 1976.

[25] Mikito Koshino and Young-Woo Son. Moiré phonons in twisted bilayer graphene. *PRB*, 100(7):075416, August 2019.

[26] R. Krishna Kumar, D. A. Bandurin, F. M. D. Pellegrino, Y. Cao, A. Principi, H. Guo, G. H. Auton, M. Ben Shalom, L. A. Ponomarenko, G. Falkovich, K. Watanabe, T. Taniguchi, I. V. Grigorieva, L. S. Levitov, M. Polini, and A. K. Geim. Superballistic flow of viscous electron fluid through graphene constrictions. *Nature Physics*, 13(12):1182–1185, December 2017.

[27] R. Krishna Kumar, X. Chen, G. H. Auton, A. Mishchenko, D. A. Bandurin, S. V. Morozov, Y. Cao, E. Khestanova, M. Ben Shalom, A. V. Kretinin, K. S. Novoselov, L. Eaves, I. V. Grigorieva, L. A. Ponomarenko, V. I. Fal'ko, and A. K. Geim. High-temperature quantum oscillations caused by recurring bloch states in graphene superlattices. *Science*, 357(6347):181–184, 2017.

[28] Mark J. H. Ku, Tony X. Zhou, Qing Li, Young J. Shin, Jing K. Shi, Claire Burch, Huiliang Zhang, Francesco Casola, Takashi Taniguchi, Kenji Watanabe, Philip Kim, Amir Yacoby, and Ronald L. Walsworth. Imaging Viscous Flow of the Dirac Fluid in Graphene Using a Quantum Spin Magnetometer. *arXiv e-prints*, page arXiv:1905.10791, May 2019.

[29] P. Kumaravadivel, M. T. Greenaway, D. Perello, A. Berdyugin, J. Birkbeck, J. Wengraf, S. Liu, J. H. Edgar, A. K. Geim, L. Eaves, and R. Krishna Kumar. Strong magnetophonon oscillations in extra-large graphene. *Nature Communications*, 10:3334, July 2019.

[30] L. D. Landau and E. M. Lifshitz. *Fluid Mechanics.* 1987.

[31] W. E. Lawrence and J. W. Wilkins. Electron-Electron Scattering in the Transport Coefficients of Simple Metals. *PRB*, 7(6):2317–2332, March 1973.

[32] Patrick J. Ledwith, Grigory Tarnopolsky, Eslam Khalaf, and Ashvin Vishwanath. Fractional Chern Insulator States in Twisted Bilayer Graphene: An Analytical Approach. *arXiv e-prints*, page arXiv:1912.09634, December 2019.

[33] Leonid Levitov and Gregory Falkovich. Electron viscosity, current vortices and negative nonlocal resistance in graphene. *Nature Physics*, 12(7):672–676, July 2016.

[34] Xiao Li, Fengcheng Wu, and S. Das Sarma. Phonon scattering induced carrier resistivity in twisted double bilayer graphene. *arXiv e-prints*, page arXiv:1906.08224, June 2019.

[35] A. H. MacDonald. Electron-Phonon Enhancement of Electron-Electron Scattering in Al. *PRL*, 44(7):489–493, February 1980.

[36] A. H. MacDonald, Roger Taylor, and D. J. W. Geldart. Umklapp electron-electron scattering and the low-temperature electrical resistivity of the alkali metals. *PRB*, 23(6):2718–2730, March 1981.

[37] Francesco M. D. Pellegrino, Iacopo Torre, and Marco Polini. Nonlocal transport and the Hall viscosity of two-dimensional hydrodynamic electron liquids. *PRB*, 96(19):195401, November 2017.

[38] V. Perebeinos, J. Tersoff, and Ph. Avouris. Phonon-Mediated Interlayer Conductance in Twisted Graphene Bilayers. *PRL*, 109(23):236604, December 2012.

[39] Hryhoriy Polshyn, Matthew Yankowitz, Shaowen Chen, Yuxuan Zhang, K. Watanabe, T. Taniguchi, Cory R. Dean, and Andrea F. Young. Large linear-in-temperature resistivity in twisted bilayer graphene. *Nature Physics*, 15(10):1011–1016, August 2019.

[40] D. G. Purdie, N. M. Pugno, T. Taniguchi, K. Watanabe, A. C. Ferrari, and A. Lombardo. Cleaning interfaces in layered materials heterostructures. *Nature Communications*, 9:5387, December 2018.

[41] A. V. Rozhkov, A. O. Sboychakov, A. L. Rakhmanov, and Franco Nori. Electronic properties of graphene-based bilayer systems. *Phys. Rep.*, 648:1–104, August 2016.

[42] Yu Kyoung Ryu, Riccardo Frisenda, and Andres Castellanos-Gomez. Superlattices based on van der waals 2d materials. *Chem. Commun.*, 55:11498–11510, 2019.

[43] Yu Saito, Tsutomu Nojima, and Yoshihiro Iwasa. Highly crystalline 2D superconductors. *Nature Reviews Materials*, 2(1):16094, February 2017.

[44] Javier D. Sanchez-Yamagishi, Jason Y. Luo, Andrea F. Young, Benjamin M. Hunt, Kenji Watanabe, Takashi Taniguchi, Raymond C. Ashoori, and Pablo Jarillo-Herrero. Helical edge states and fractional quantum Hall effect in a graphene electron-hole bilayer. *Nature Nanotechnology*, 12(2):118–122, February 2017.

[45] M. Serlin, C. L. Tschirhart, H. Polshyn, Y. Zhang, J. Zhu, K. Watanabe, T. Taniguchi, L. Balents, and A. F. Young. Intrinsic quantized anomalous Hall effect in a moiré heterostructure. *Science*, 367(6480):900–903, February 2020.

[46] Girish Sharma, Indra Yudhistira, Nilotpal Chakraborty, Derek Y. H. Ho, Michael S. Fuhrer, Giovanni Vignale, and Shaffique Adam. Carrier transport theory for twisted bilayer graphene in the metallic regime. *arXiv e-prints*, page arXiv:2003.00018, February 2020.

[47] Aaron L. Sharpe, Eli J. Fox, Arthur W. Barnard, Joe Finney, Kenji Watanabe, Takashi Taniguchi, M. A. Kastner, and David Goldhaber-Gordon. Emergent ferromagnetism near three-quarters filling in twisted bilayer graphene. *Science*, 365(6453):605–608, August 2019.

[48] Thibault Sohier, Matteo Calandra, Cheol-Hwan Park, Nicola Bonini, Nicola Marzari, and Francesco Mauri. Phonon-limited resistivity of graphene by first-principles calculations: Electron-phonon interactions, strain-induced gauge field, and Boltzmann equation. *PRB*, 90(12):125414, September 2014.

[49] Joseph A. Sulpizio, Lior Ella, Asaf Rozen, John Birkbeck, David J. Perello, Debarghya Dutta, Moshe Ben-Shalom, Takashi Taniguchi, Kenji Watanabe, Tobias Holder, Raquel Queiroz, Alessandro Principi, Ady Stern, Thomas Scaffidi, Andre K. Geim, and Shahal Ilani. Visualizing Poiseuille flow of hydrodynamic electrons. *Nature*, 576(7785):75–79, December 2019.

[50] Thiti Taychatanapat, Kenji Watanabe, Takashi Taniguchi, and Pablo Jarillo-Herrero. Electrically tunable transverse magnetic focusing in graphene. *Nature Physics*, 9(4):225–229, April 2013.

[51] Iacopo Torre, Andrea Tomadin, Andre K. Geim, and Marco Polini. Non-local transport and the hydrodynamic shear viscosity in graphene. *PRB*, 92(16):165433, October 2015.

[52] L. Wang, I. Meric, P. Y. Huang, Q. Gao, Y. Gao, H. Tran, T. Taniguchi, K. Watanabe, L. M. Campos, D. A. Muller, J. Guo, P. Kim, J. Hone, K. L. Shepard, and C. R. Dean. One-Dimensional Electrical Contact to a Two-Dimensional Material. *Science*, 342(6158):614–617, November 2013.

[53] Matthew Yankowitz, Shaowen Chen, Hryhoriy Polshyn, Yuxuan Zhang, K. Watanabe, T. Taniguchi, David Graf, Andrea F. Young, and Cory R. Dean. Tuning superconductivity in twisted bilayer graphene. *Science*, 363(6431):1059–1064, March 2019.

[54] Matthew Yankowitz, Qiong Ma, Pablo Jarillo-Herrero, and Brian J. LeRoy. van der Waals heterostructures combining graphene and hexagonal boron nitride. *Nature Reviews Physics*, 1(2):112–125, January 2019.

[55] A. F. Young, J. D. Sanchez-Yamagishi, B. Hunt, S. H. Choi, K. Watanabe, T. Taniguchi, R. C. Ashoori, and P. Jarillo-Herrero. Tunable symmetry breaking and helical edge transport in a graphene quantum spin Hall state. *Nature*, 505(7484):528–532, January 2014.

[56] Noah F. Q. Yuan, Hiroki Isobe, and Liang Fu. Magic of high-order van Hove singularity. *Nature Communications*, 10:5769, December 2019.

[57] Indra Yudhistira, Nilotpal Chakraborty, Girish Sharma, Derek Y. H. Ho, Evan Laksono, Oleg P. Sushkov, Giovanni Vignale, and Shaffique Adam. Gauge-phonon dominated resistivity in twisted bilayer graphene near magic angle. *PRB*, 99(14):140302, April 2019.

[58] Mohammad Zarenia, Indra Yudhistira, Shaffique Adam, and Giovanni Vignale. Enhanced hydrodynamic transport in near magic angle twisted bilayer graphene. *PRB*, 101(4):045421, January 2020.

[59] W. Zhang, M. A. Zudov, L. N. Pfeiffer, and K. W. West. Resonant phonon scattering in quantum hall systems driven by dc electric fields. *Phys. Rev. Lett.*, 100:036805, Jan 2008.

[60] Ya-Hui Zhang and T. Senthil. Quantum Hall spin liquids and their possible realization in moiré systems. *arXiv e-prints*, page arXiv:2003.13702, March 2020.